



## A new high-resolution unstructured grid finite volume Arctic Ocean model (AO-FVCOM): An application for tidal studies

Changsheng Chen,<sup>1,2</sup> Guoping Gao,<sup>1,3</sup> Jianhua Qi,<sup>1</sup> Andrey Proshutinsky,<sup>4</sup> Robert C. Beardsley,<sup>4</sup> Zygmunt Kowalik,<sup>5</sup> Huichan Lin,<sup>1</sup> and Geoffrey Cowles<sup>1</sup>

Received 12 June 2008; revised 9 March 2008; accepted 28 April 2009; published 27 August 2009.

[1] A spherical coordinate version of the unstructured grid 3-D FVCOM (finite volume coastal ocean model) has been applied to the Arctic Ocean to simulate tides with a horizontal resolution ranging from 1 km in the near-coastal areas to 15 km in the deep ocean. By accurately resolving the irregular coastlines and bathymetry in the Arctic Ocean coastal regions, this model reproduces the diurnal ( $K_1$  and  $O_1$ ) and semidiurnal ( $M_2$  and  $S_2$ ) tidal wave dynamics and captures the complex tidal structure along the coast, particularly in the narrow straits of the Canadian Archipelago. The simulated tidal parameters (harmonic constituents of sea surface elevation and currents) agree well with the available observational data. High-resolution meshes over the continental shelf and slope capture the detailed spatial structure of topographic trapped shelf waves, which are quite energetic along the Greenland, Siberia, and Spitsbergen continental slope and shelf break areas. Water stratification influences the vertical distribution of tidal currents but not the water transport and thus tidal elevation. The comparison with previous finite difference models suggests that horizontal resolution and geometric fitting are two prerequisites to simulate realistically the tidal energy flux in the Arctic Ocean, particularly in the Canadian Archipelago.

**Citation:** Chen, C., G. Gao, J. Qi, A. Proshutinsky, R. C. Beardsley, Z. Kowalik, H. Lin, and G. Cowles (2009), A new high-resolution unstructured grid finite volume Arctic Ocean model (AO-FVCOM): An application for tidal studies, *J. Geophys. Res.*, 114, C08017, doi:10.1029/2008JC004941.

### 1. Introduction

[2] Numerical modeling has become one of the major tools for understanding past conditions and for explaining recent observed changes in the Arctic Ocean. A state-of-the-art Arctic Ocean model requires (1) grid flexibility to resolve the complex coastline and steep continental slopes, (2) mass conservation to accurately simulate mass, heat and salt transports, (3) proper parameterization of vertical and lateral mixing, (4) advanced data assimilation methods to integrate observations with simulation results, and (5) modular design to facilitate selection and/or addition of essential model components needed in both process-oriented and hindcast/forecast application. The Arctic Ocean Model Intercomparison (AOMIP) [Proshutinsky *et al.*, 2001, 2005; Proshutinsky

and Kowalik, 2007] studies have shown that at least two obvious improvements are needed for Arctic regional models: (1) increasing model horizontal and vertical resolution [Panteleev *et al.*, 2007; Golubeva and Platov, 2007] and (2) including tidal motions in the model dynamics for more realistic simulation of water vertical/lateral mixing and tide-ice interactions [Proshutinsky, 1993; Kowalik and Proshutinsky, 1994, hereafter referred as KP; Holloway and Proshutinsky, 2007].

[3] The first improvement is aimed at resolving the Arctic Ocean fluid dynamical and thermal processes over complex coastal geometry, steep continental slopes and deep ridges. In the Canadian Archipelago, for example, numerous islands are separated by narrow water passages with widths of approximately 5 km or less (Figure 1). Since these passages function as a network for water, ice and tidal energy exchange between the Arctic and North Atlantic Oceans, resolving these passages is critical for Arctic Ocean modeling. This was demonstrated by Joyce and Proshutinsky [2007], who pointed out that the failure to resolve the real widths of the Canada Straits in a model can cause either overestimation or underestimation of the magnitude of the inflow of Atlantic water to the Arctic Ocean via Fram Strait and the Barents Sea opening and thus influence the recirculation of the surface waters and freshwater fluxes around Greenland.

[4] The second improvement can play a role in shaping the Arctic's climate. Vertical mixing is dominated by the

<sup>1</sup>Department of Fisheries Oceanography, School for Marine Science and Technology, University of Massachusetts-Dartmouth, New Bedford, Massachusetts, USA.

<sup>2</sup>Also at Marine Ecosystem and Environmental Laboratory, Shanghai Ocean University, Shanghai, China.

<sup>3</sup>Department of Physical Oceanography, Ocean University of China, Qingdao, China.

<sup>4</sup>Department of Physical Oceanography, Woods Hole Oceanographic Institution, Woods Hole, Massachusetts, USA.

<sup>5</sup>Institute of Marine Science, University of Alaska Fairbanks, Fairbanks, Alaska, USA.

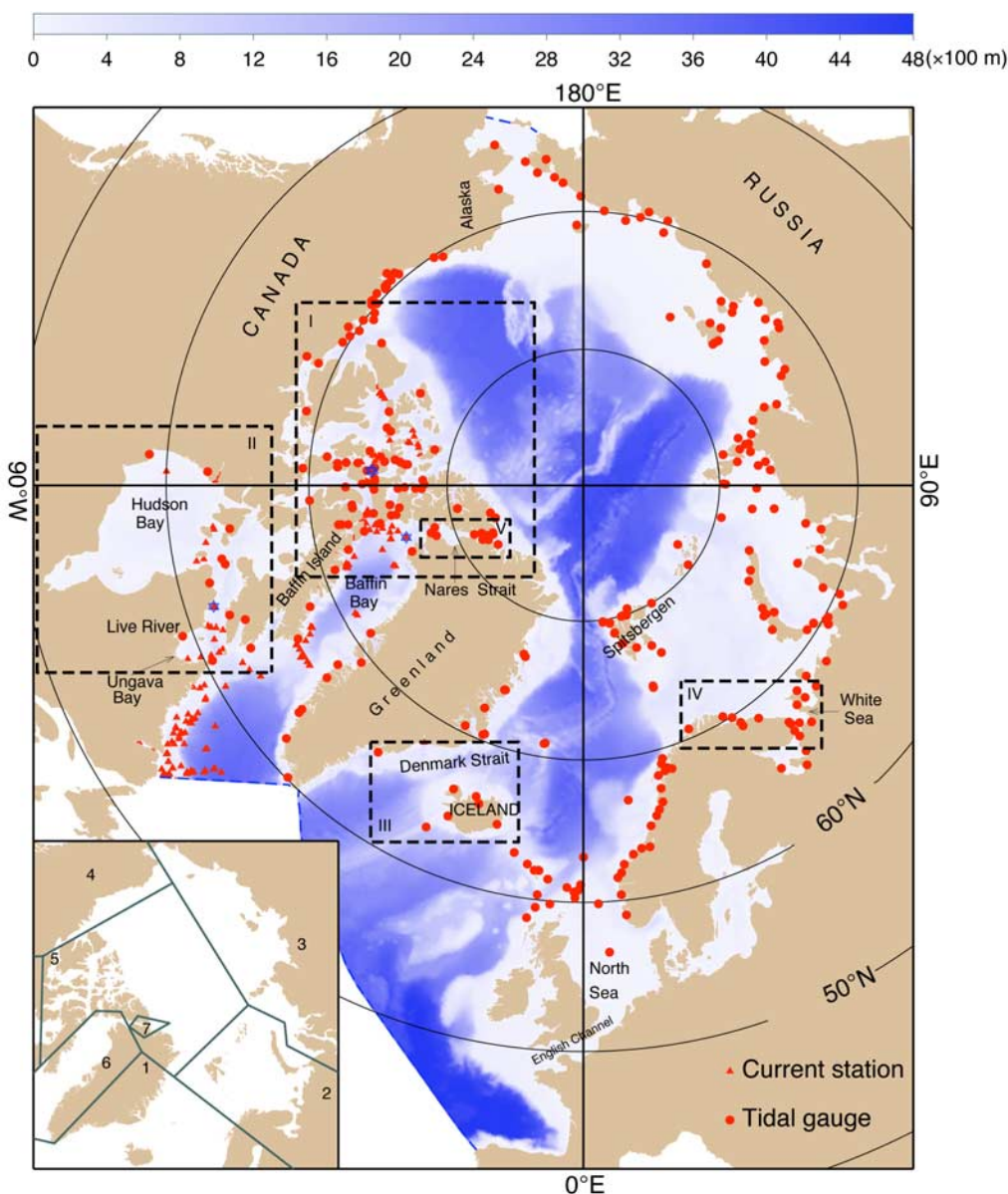


**Figure 1.** Bathymetry (in meters) of the Arctic Ocean and locations of tide gauges (dots) and current mooring/buoys (triangles). Total numbers of tide gauge and mooring stations are 297 and 416, respectively. Tide gauge data were downloaded from <http://www.ims.uaf.edu/tide/> and from *Kowalik and Proshutinsky* [1993, 1994, 1995]; the current data were downloaded from <http://www.mar.dfo-mpo.gc.ca/science/ocean/>. Boxes with dashed lines are five subdivisions selected for model-data comparisons of tidal elevation: region I, the Canadian Archipelago; region II, Hudson Bay/Strait; region III, Denmark Strait/Iceland; region IV, the White Sea; and region V, Nares Strait. The subregions defined by PE are shown in the inset as 1–7. The measurement sites used for the comparison of model-predicted and observed vertical profiles of tidal current ellipses are indicated using blue stars. The sites inside Hudson Bay and Baffin Bay are marked as “A” and “B,” respectively, while the sites in the Canadian Archipelago are marked as “C” and “D.” C and D are very close to each other.

wind at the surface but by tides over continental slopes [Munk and Wunsch, 1998]. In regions covered by ice and especially by landfast ice, the tides could be a force producing vertical mixing at the surface between ice and ocean [Padman and Dillon, 1991; Zakharchuk, 1999; St. Laurent and Garrett, 2002; Wang *et al.*, 2003; Holloway and Proshutinsky, 2007; St. Laurent, 2008]. An example of tidal mixing impacts on sea ice was given by Wang *et al.*

[2003] in Hudson Bay. Comparing model simulations for cases with and without tides, they reported that the case without tides produced  $\sim 38\%$  more sea ice. The tidal contribution to the ice cover and thickness is evident in recent tidal current measurements in Hudson Bay by St. Laurent [2008]. Tides produce mixing and heat flux anomalies required for polynya formation, so that an underestimate of tide-induced heat exchange at the surface can cause an

increase of ice cover. This finding is supported in a coupled ocean-ice model experiment by *Holloway and Proshutinsky* [2007], who showed that the tide-enhanced heat loss from the Atlantic Water leads to a spatial difference of the ice thickness along continental slopes and in the interior of the basin. Internal tides are energetic over supercritical topography at the shelf break [*St. Laurent and Garrett*, 2002]. They cover a wide wave number spectrum, with low modes radiating away from the shelf and with high modes supporting local mixing. Internal tides have an impact on the water transport [*Schiller*, 2004] and distributions of water temperature and salinity [*D'Asaro and Morison*, 1992; *Muench et al.*, 1996; *Padman*, 1995; *Robertson*, 2001] as well as enhance tidal mixing over slope and reduction of the ice thickness [*Holloway and Proshutinsky*, 2007].

[5] Our present knowledge of tides in the Arctic Ocean is based on coastal observations and numerical models. The semidiurnal  $M_2$  and  $S_2$  and diurnal  $K_1$  and  $O_1$  tidal waves dominate variations in tidal elevation and currents in the Arctic Ocean. Tidal mixing and stirring are especially strong along the Eurasian Shelf. In the Barents Sea, strong tidal currents are observed around Spitsbergenbanken, Bear and Hopen Islands [*Huthnance*, 1981; *Nilsen et al.*, 1990; *Pease et al.*, 1995; KP]. At the entrance to the White Sea, the tidal currents are often up to 200 cm/s. Along the Siberian Shelf, especially in the vicinity of New Siberian Islands, the tidal currents reach up to 50 cm/s. The tidal currents along the Alaska Beaufort coast are in the order of 5–10 cm/s, but can be enhanced in the narrow entrances to coastal lagoons. Tidal currents were also observed in the vicinity of the North Pole [*Aagaard*, 1981]. *Kwok et al.* [2004] demonstrated that tides and near-inertial motion might contribute to sea ice deformation in the central Arctic far away from coastal regions where tidal currents are strong.

[6] Previous tidal simulations for the Arctic Ocean were made using structured grid finite difference models. Highly referenced works are *Kowalik and Proshutinsky* [1993, 1994, 1995] and *Padman and Erofeeva* [2004] (hereafter referred to as PE). KP developed a two-dimensional (2-D) (vertically averaged) fully nonlinear barotropic Arctic tidal model with sea ice. With a uniform horizontal resolution of 13.89 km and proper parameterization of the bottom friction, this model provided a reasonable simulation of tidal elevation around the Arctic Ocean and described tidal effects in the sea ice cover. The 2-D assumption and horizontal resolution specified in the KP model, however, limit its application to resolve the 3-D current features and complex tidal energy exchange between the Arctic and Atlantic Ocean through the Canadian Archipelago. PE introduced a 2-D linear tidal model (AODIM—the Arctic Ocean tide inverse model) to assimilate the tidal elevation in the Arctic Ocean by computing the inverse solution with all available tidal gauge data. With a horizontal resolution of 5 km, the inverse assimilated tidal elevation shows a better match with observations with smaller overall standard deviation errors. In addition to the 2-D limitation, the linear assumption used by PE, however, makes this model incapable of resolving residual currents and tide-induced water transports in coastal regions where the interaction of tidal currents with topography is highly nonlinear. Although PE's horizontal grid spacing is  $\sim 3$  times smaller than that in KP's

model, it is still insufficient to resolve the complex geometry within the Canadian Archipelago.

[7] To satisfy the need for an improved model for Arctic Ocean research, we have applied the unstructured grid Finite-Volume Coastal Ocean Model (FVCOM) to the Pan-Arctic region (hereafter referred as AO-FVCOM). FVCOM is a fully nonlinear prognostic, free-surface hydrostatic 3-D model in which the primitive equations are solved numerically using the finite volume flux approach with guarantee of local conservation of mass, momentum, heat, and tracers [*Chen et al.*, 2003; *Chen et al.*, 2006a, 2006b, 2007; *Cowles*, 2008]. The model is discretized with an unstructured triangular grid in the horizontal and the generalized terrain-following coordinate in the vertical [*Pietrzak et al.*, 2002]. Geometrical flexibility of the unstructured grid allows us to construct triangular meshes without restriction from the meridional convergence of latitude and longitude and any need for “grid rotation.” The singularity at the North Pole is removed by using a spherical-polar stereographic projection nested grid at the pole. To validate the capability of this model to capture Arctic Ocean dynamics, we have first applied it to simulate the tides in a barotropic and stratified ice-free Arctic Ocean including Baffin Bay and Hudson Bay/Strait. The model evaluation was made by comparing it with observational data and presently available tidal models in the Arctic Ocean.

[8] The paper is structured as follows. AO-FVCOM and the design of the numerical experiments are described in section 2. Model verification results are presented in section 3. Tidal energetics and mixing are discussed in section 4. Discussions and intermodel comparisons are given in section 5 and conclusions are summarized in section 6.

## 2. Model Description

[9] The AO-FVCOM is a spherical coordinate version of FVCOM that has been developed and configured for Arctic Ocean applications. In common with other free-surface coastal models, FVCOM uses the modified Mellor and Yamada level 2.5 and Smagorinsky turbulent closure schemes as default setups for vertical and horizontal mixing, respectively [*Mellor and Yamada*, 1982; *Galperin et al.*, 1988; *Smagorinsky*, 1963]. The FVCOM version used in this study is numerically solved by a mode splitting method. The external mode is composed of vertically integrated transport equations in which the water elevation is solved explicitly using a shorter time step constrained by the ratio of the horizontal resolution to the phase speed of the surface gravity wave. The internal mode consists of the fully 3-D governing equations and is solved using a longer time step constrained by the phase speed of the lowest mode internal wave. Linkage between external and internal modes is through the surface elevation, with mode adjustments at each internal time step. Unlike finite difference and finite element models, FVCOM solves the flux form of the governing equations in unstructured triangular volumes by a second-order accurate discrete flux scheme. The finite volume approach used in the model not only takes advantage of finite element methods in geometric flexibility and finite difference methods in computational efficiency, but also provides a more accurate numerical representation of

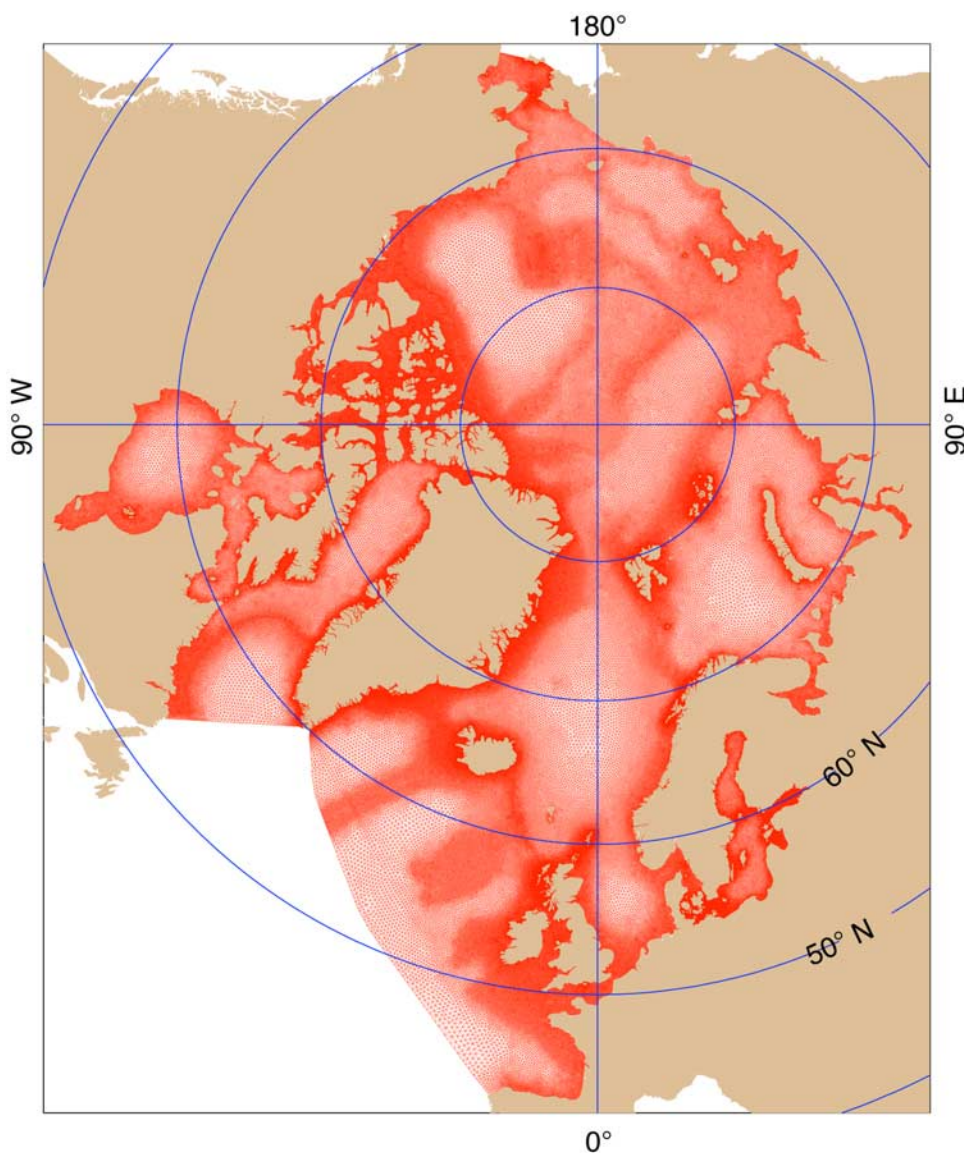


**Figure 2.** Unstructured triangular grid of AO-FVCOM for the Arctic Ocean. Total numbers of triangular cells and nodes are 520,817 and 275,574. The horizontal resolution (measured by the side length of each triangle) varies from 1 to 3 km in the Canadian Archipelago, inlets and straits, and over the shelf break to 10–15 km in the interior basins.

mass, momentum, heat, and salt conservation in the computational domain.

[10] The computational domain of AO-FVCOM covers the entire Arctic Ocean including the Canadian Archipelago, Hudson and Baffin Bays, the Labrador, Greenland, and Norwegian Seas, and the Denmark Strait (Figure 2) and is bounded by three open boundaries across the Labrador and Greenland Seas in the Atlantic Ocean and across the Bering Strait connected to the Pacific Ocean. In the horizontal, the domain is configured with an unstructured triangular grid with a resolution varying from 1 km in the Canadian Archipelago, inlets and straits, and in and over the shelf break region, to 10–15 km in the deep ocean basins. Total numbers of triangular cells and nodes are 520,817 and 275,574. In the vertical, the domain is divided into 40 nonuniform  $\sigma$  layers, which corresponds to a vertical resolution of 1–10 m or less in the coastal region (where

the water depth is shallower than 300 m) and about 10 m near the surface and bottom in the deep ocean basins (where the water is deeper than 4000 m). The minimum water depth in the model was 5 m (applied along all coastlines).

[11] The bathymetric data were taken from two sources: the sub-Arctic region (up to 72°N) is represented by depths from the 2-min Naval Oceanographic Office Digital Bathymetric Data Base–Variable resolution (DBDBV) version 4.3 and the central Arctic bathymetry is obtained from The International Bathymetric Chart of the Arctic Ocean (IBCAO), a digital database that contains all available bathymetric data north of 64°N. These two data sets match very well in the overlapping region between 64°N and 72°N. In the “barotropic” configuration (defined here as the full 3-D model with homogeneous fluid), AO-FVCOM is forced by tidal elevations prescribed at the open boundaries. Model equations include astronomical forcing implemented via

gradients of the tide-generating potential for each tidal constituent and various corrections due to the Earth tide and ocean loading (see KP for details). In the “stratified” configuration, the model is forced by the same tidal forcing but with the initial temperature and salinity fields specified using the summer fields of hydrographic climatology (PHC3.0) downloaded from the Polar Science Center, Applied Physics Laboratory/University of Washington.

[12] Four major tidal waves are investigated: two semidiurnal ( $M_2$  and  $S_2$ ) and two diurnal ( $K_1$  and  $O_1$ ). The amplitudes and phases of these constituents at open boundaries are specified using the inverse global tidal model output (TPXO6.2) with adjustment to reach an overall minimum root-mean-square error relative to the available tidal gauge measurements in the computational domain (Figure 1). Initial model simulations conducted using the tidal elevation constructed from the TPXO6.2 output on the open boundary showed spatially uniform errors in the model-computed tidal amplitudes and phases in some coastal regions that were clearly related to the tidal forcing on the open boundary. We believe that these errors were caused by inaccuracies in the tidal boundary forcing produced by TPXO6.2 due to the lack of field data. We then made small adjustments to the tidal amplitudes and phases on the open boundary to minimize these errors within the model domain.

[13] The tidal simulations were run for more than 100 days, with the tidal elevation and currents reaching a quasi-equilibrium state after 40 model days. The time step used in this model is 6 s for the external mode and 60 s for the internal mode.

[14] The model results are compared with tidal constituent parameters computed using time series measurements made in the computational domain (Figure 1). Total number of tide gauge sites is 297; these data were downloaded from <http://www.ims.uaf.edu/tide/> prepared and provided by *Kowalik and Proshutinsky* [1993, 1994, 1995]. Total number of current measurement sites is 234, which include 934 time series of current at different depths. Most of these sites were located in the Labrador Sea, Hudson Bay, and Canadian Archipelago (Figure 1). (The current data were downloaded from the Data Management and Services, Ocean Science Division, Fisheries and Oceans Canada, Bedford Institute of Oceanography, Canada Web site <http://www.mar.dfo-mpo.gc.ca/science/ocean/>)

### 3. Results of Tidal Simulations

#### 3.1. Barotropic Tidal Elevation

[15] The AO-FVCOM simulated tidal amplitudes, phases and number of amphidromic points (nodes) (Figure 3) are in general agreement with previous results presented by KP and PE. Some discrepancies, however, occur among the AO-FVCOM, KP and PE results. For example, the central Arctic  $M_2$  node in the AO-FVCOM cotidal chart (Figure 3) is shifted to the west relative to the KP and PE locations of this node. There are also a number of additional nodes in the AO-FVCOM results in comparison with the KP and PE charts. This is understandable because AO-FVCOM resolves the complex coastline and bathymetry better than the PE model and much better than the KP model. The mutual interactions between incoming waves and those reflected from the complex coastline and bathymetry in AO-FVCOM naturally results in the generation of second-

ary nodes in the coastal areas. While the severe lack of observational data does not allow us to confirm the existence of these nodes, the coastal tide gauge information can be used to verify model results at least along the coastline.

[16] The semidiurnal  $M_2$  and  $S_2$  cotidal charts show similar distributions of amplitude and phase (Figure 3). The semidiurnal tides are relatively small in the deep Arctic basins and larger in the Hudson Strait/Bay, southern Baffin Bay, the Denmark Strait west of Iceland, and the White Sea. Numerous nodes occur along (or near to) the coast, indicating that the semidiurnal tidal phases at two very close locations can differ significantly. The diurnal  $K_1$  and  $O_1$  tidal amplitudes are of order 10 times smaller than the semidiurnal tidal amplitudes. These diurnal tides have similar horizontal patterns in amplitude but different phase distributions (Figure 3). Both  $K_1$  and  $O_1$  diurnal tidal waves are characterized by trains of trapped shelf waves around Greenland and along the Siberian shelf break as first described by KP. However, the AO-FVCOM cotidal charts reveal additional locations for this phenomenon due to its much higher grid resolution than that used in KP. The model  $K_1$  and  $O_1$  phases differ significantly in the Greenland Sea and Arctic Basin. For example, around Spitsbergen Island, the  $K_1$  tide exhibits one amphidromic point on the southwest and three amphidromic points on the south side while the  $O_1$  tide has no amphidromic points in these two areas. Along the Alaskan coast, the  $K_1$  has many amphidromic points while the  $O_1$  has only one.

[17] The AO-FVCOM tidal amplitudes and phases were compared with in situ tide gauge results as one test of the present model. This model-data comparison was made at 257 tidal gauge sites selected from the 297 available sites (40 sites were rejected due to either being located out of the computational domain or because of bad data quality). The overall root-mean-square (RMS) differences between model and observed tidal amplitudes and phases for the four main constituents are listed in Table 1. The model provides reasonable agreement with the tide gauge results in amplitude but not in phase. The relatively large phase differences between modeled and observed diurnal tides were caused by the model errors along the Russian and Canadian coasts, which we think are due in part to inaccurate bathymetry data in these regions and the effects of fast ice in coastal areas that were not included in the AO-FVCOM barotropic simulation. The influence of the fast ice was taken into account by adding additional friction over the shallow water region of  $<20$  m in KP, which did show an improvement in the model-data comparison for tidal elevation. Model-data comparisons at individual tide gauge sites plus the high-resolution semidiurnal and diurnal cotidal charts are shown in Data Sets S1–S4 and Figures S1–S4 in the auxiliary material.<sup>1</sup>

[18] We selected five regions (defined in Figure 1) to check model performance in different tidal regimes in the Arctic. The model-data comparisons for these five regions are listed in Table 2 and presented next.

##### 3.1.1. Region I: Canadian Archipelago

[19] This area contains numerous islands that are separated by narrow and deep straits. The bathymetry of this

<sup>1</sup>Auxiliary material data sets are available at <ftp://ftp.agu.org/apend/jc/2008/jc004941>. Other auxiliary material files are in the HTML.

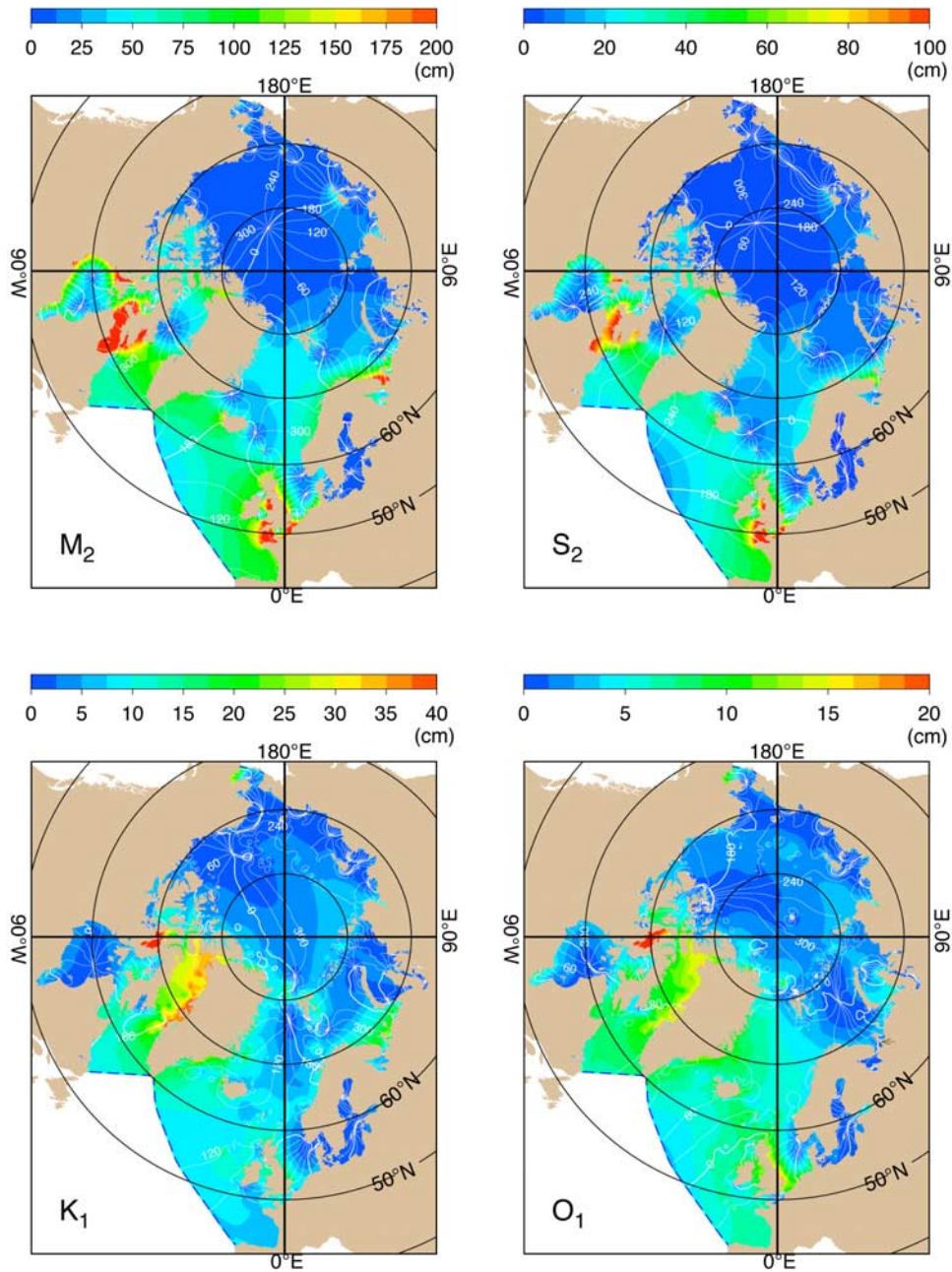


**Figure 3.** The model-predicted  $M_2$ ,  $S_2$ ,  $K_1$ , and  $O_1$  cotidal charts. The color image represents the tidal amplitude (cm) and contours indicate the tidal phase (degrees Greenwich time,  $^{\circ}G$ ).

region is not well known because of the thick landfast and pack ice. The model tidal amplitudes vary significantly in this region from a few to over 150 cm. On the basis of the 76 tide gauge station data, the RMS difference in amplitude relative to the observed maximum value is  $\sim 5\text{--}6\%$  for the  $M_2$  and  $S_2$  tides,  $\sim 4\%$  for the  $K_1$  tide and  $7\%$  for the  $O_1$  tide. The model-computed tidal phases are in reasonable agreement with the tide gauge data for the semidiurnal tides but not for the diurnal tides. The RMS error is  $12.7^{\circ}$  for  $M_2$  and  $S_2$ , but  $38.4^{\circ}$  and  $26.7^{\circ}$  for  $K_1$  and  $O_1$ . Converting the phase lag errors to time, the model showed a time lag of  $\sim 26$  min for  $M_2$  and  $S_2$ , but 2.7 h for  $K_1$  and 1.9 h for  $O_1$ .

**Table 1.** Comparison Between Model-Computed and Observed Tidal Elevations at 257 Tidal Gauges Under the Homogenous Condition

Tidal Constituent	Model-Data Elevation					
	Difference		Absolute Difference		Root Mean Square	
	Amplitude (cm)	Phase <sup>a</sup> ( $^{\circ}G$ )	Amplitude (cm)	Phase <sup>a</sup> ( $^{\circ}G$ )	Amplitude (cm)	Phase <sup>a</sup> ( $^{\circ}G$ )
$M_2$	0.7	-4.0	4.3	11.1	6.5	14.4
$S_2$	-0.3	-1.1	2.3	12.5	4.0	18.6
$K_1$	0.0	-12.5	2.0	26.6	2.8	41.4
$O_1$	0.3	-6.3	1.1	24.5	1.5	41.5

<sup>a</sup>In degrees Greenwich time.

**Table 2.** Comparison Between Model-Computed and Observed Semidiurnal Tidal Elevations in Five Selected Regions Shown in Figure 1 Under the Homogeneous Condition

Tidal Constituent	Observed Elevation Mean (cm)	Observed Maximum Elevation (cm)	Amplitude Error (cm)		Phase Error ( $^{\circ}$ G)	
			Absolute Difference	Root Mean Square	Absolute Difference	Root Mean Square
<i>Canadian Archipelago, Station 76</i>						
M <sub>2</sub>	41.6	116.7	4.3	5.8	10.0	12.7
S <sub>2</sub>	16.4	48.1	1.6	2.2	9.3	12.7
K <sub>1</sub>	15.4	63.7	2.7	3.6	27.6	38.4
O <sub>1</sub>	6.8	27.6	1.4	1.8	17.7	26.7
<i>Hudson Strait/Bay, Station 9</i>						
M <sub>2</sub>	228.9	429.0	8.7	18.1	13.6	18.4
S <sub>2</sub>	70.2	136.0	8.3	11.4	13.6	16.6
K <sub>1</sub>	13.0	19.0	3.7	4.5	32.0	42.3
O <sub>1</sub>	6.7	9.0	1.7	2.4	24.3	32.1
<i>Denmark Strait and Around Iceland, Station 7</i>						
M <sub>2</sub>	78.0	132.0	6.0	6.7	3.1	3.8
S <sub>2</sub>	28.6	51.0	2.3	2.7	16.4	30.7
K <sub>1</sub>	9.5	14.0	1.7	2.1	5.7	6.7
O <sub>1</sub>	5.2	7.0	1.5	2.7	15.0	18.8
<i>White Sea, Station 9</i>						
M <sub>2</sub>	116.9	274.0	5.3	6.5	8.3	9.4
S <sub>2</sub>	30.1	51.0	7.7	12.1	14.7	19.9
K <sub>1</sub>	11.3	18.0	1.9	2.2	36.6	45.6
O <sub>1</sub>	2.5	3.0	0.2	0.3	22.4	23.3
<i>Nares Strait, Station 14</i>						
M <sub>2</sub>	57.8	116.7	2.4	2.8	11.2	12.1
S <sub>2</sub>	24.9	48.1	1.0	1.7	8.2	9.8
K <sub>1</sub>	13.5	34.4	2.8	3.6	6.2	8.2
O <sub>1</sub>	5.3	13.1	1.2	1.5	6.2	7.4

### 3.1.2. Region II: Hudson Strait and Hudson Bay

[20] On the basis of the nine tide gauge stations in this region, the semidiurnal tides dominate, with maximum amplitudes of 429 cm for the M<sub>2</sub> tide and 136 cm for the S<sub>2</sub> tide. The diurnal tides in this region are relatively weak, with maximum amplitudes of 19 cm for the K<sub>1</sub> tide and 9 cm for the O<sub>1</sub> tide. The RMS amplitude difference relative to the observed maximum value is 4.3% for the M<sub>2</sub> tide and 7.0% for the S<sub>2</sub> tide. Although the RMS differences of model-predicted and observed amplitudes for K<sub>1</sub> and O<sub>1</sub> tides are relatively larger compared with the maximum observed values, they are insignificant to the total tidal elevation in such a region dominated by semidiurnal tides. The phase errors for both semidiurnal and diurnal tides are similar to those in region I.

### 3.1.3. Region III: Denmark Strait

[21] This is the other region that features relatively large M<sub>2</sub> tidal amplitude. On the basis of the seven tide gauge stations in this region, the maximum tidal amplitude is  $\sim 183$  cm for semidiurnal tides (a sum of M<sub>2</sub> and S<sub>2</sub> tides) and  $\sim 21$  cm for diurnal tides (a sum of K<sub>1</sub> and O<sub>1</sub> tides). The model-computed M<sub>2</sub> tidal amplitude and phase agree well with the tide gauge data with a RMS amplitude difference relative to the observed maximum value of  $\sim 5.1\%$  and  $3.8^{\circ}$  RMS phase difference. The S<sub>2</sub> exhibits a similar RMS amplitude difference but larger RMS phase difference. The model-computed diurnal tidal amplitudes have a similar accuracy but the diurnal phases differences are still significant although smaller than in regions I, II and IV.

### 3.1.4. Region IV: White Sea

[22] This is an area with large semidiurnal tides in the Arctic Ocean. On the basis of the nine tide gauge stations in this region, the maximum tidal amplitude is  $\sim 325$  cm for

the semidiurnal tides (a sum of M<sub>2</sub> and S<sub>2</sub>) and  $\sim 21$  cm for the diurnal tides (a sum of K<sub>1</sub> and O<sub>1</sub>). The AO-FVCOM model is capable of reproducing the maximum tidal elevation in this region. For example, at MEZEN2 station ( $44^{\circ}$ E,  $66.1667^{\circ}$ N), the model predicts a maximum tidal elevation of 276.6 cm, which is only 2.6 cm higher than that measured. Except at two stations inside the White Sea, the model-data amplitude difference for the M<sub>2</sub> tide is  $\leq 3$  cm, even though the RMS model-data amplitude and phase differences (based on all stations) listed in Table 2 are 6.5 cm and  $9.4^{\circ}$ . The RMS amplitude and phase differences for the S<sub>2</sub> tide are roughly twice as large as those for the M<sub>2</sub> tide. Compared with the tide gauge data, the model-computed diurnal tidal constants exhibit small RMS differences in amplitude but large differences in phase.

### 3.1.5. Region V: Nares Strait

[23] This channel connects Baffin Bay with the Arctic Ocean. The field data show that the M<sub>2</sub> tidal elevation decreases gradually from  $\sim 110$  cm in Baffin Bay to  $\sim 20$  cm in the Arctic Ocean, with a maximum value of 117 cm. The M<sub>2</sub> phase difference between the southern and northern ends of this strait is  $\sim 40^{\circ}$ . These features of the M<sub>2</sub> tidal wave propagation are captured well by the AO-FVCOM simulation. The model also shows reasonable agreement in amplitude and phase for both semidiurnal and diurnal tides.

[24] The largest RMS differences between the AO-FVCOM and tide gauge data are observed along the Russian coast. It is important to note that the tidal elevation data used in the model-data comparison were taken from the KP database and that the most ( $\sim 80\%$ ) of these data came from tide tables (1941) published in Russia before World War II and their quality has never been evaluated and discussed. Recently, some reanalysis of the tidal sea level harmonic constants was done for the Kara Sea at the Arctic and Antarctic Research

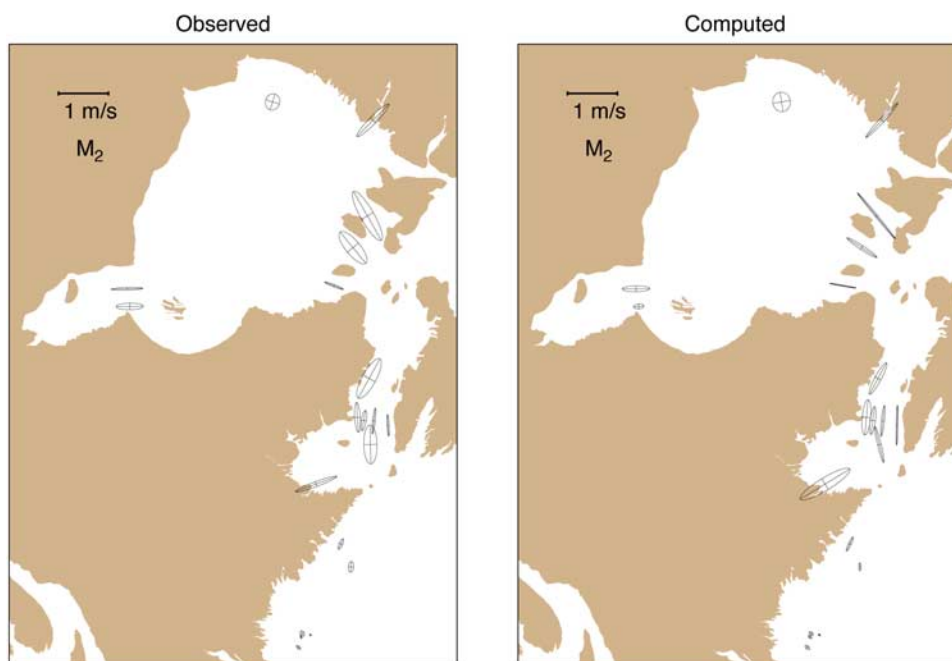


**Figure 4.** Comparison between (left) observed and (right) model-computed  $M_2$  tidal current ellipses at measurement depths on moorings in Hudson Bay/Strait. The measurement depths at those sites differed and are given in Data Set S5 in the auxiliary material.

Institute (AARI) [Voinov, 2002]. Results revealed that significant corrections (both in amplitude and phase) are needed for many coastal stations. Thus the misfit between AO-FVCOM and the data might be, at least in part, due to errors in the tabulated harmonic coefficients for these tide stations.

### 3.2. Barotropic Tidal Currents

[25] The AO-FVCOM semidiurnal tidal currents are strong in Hudson Strait/Bay, southern part of Baffin Bay, Denmark Strait, White Sea, and Nares Strait where the tidal elevations are large, and weak in the Arctic Basin where tidal elevations are small and the mean depth greater. In Hudson Strait/Bay, for example, the model shows that maximum  $M_2$  tidal currents exceed 200 cm/s, with ellipses parallel to the local coastlines or bottom slope. In the Canadian Archipelago, the  $M_2$  tidal currents vary significantly in space. The tidal currents are relatively weak in wider passages but they can reach or exceed 100 cm/s in some narrow channels. Diurnal tidal currents are generally a factor of  $\sim 10$  smaller than the  $M_2$  tidal current in the near-resonant semidiurnal tidal regions, but they are comparable with the  $M_2$  tidal current in many coastal areas around the Arctic Ocean. In Baffin Bay, for example, the  $K_1$  tidal currents can exceed 20 cm/s along the eastern slope, which are of order of the  $M_2$  tidal currents in that region. In the Canadian Archipelago, the  $K_1$  tidal currents in some narrow channels reach 40–50 cm/s, which are also comparable with the  $M_2$  tidal current in those areas. Consistent with the tidal elevation pattern, the diurnal tidal currents are generally stronger at the margin of the continental shelf where bottom topography is steep. The orientations of the diurnal tidal current ellipses are topographically controlled, with a tendency to align with the local bottom slope. These features are clearly evident on the eastern shelves of Baffin Bay and Greenland and around Spitsbergen in the model results

when the tidal current ellipses are plotted together with local isobaths.

[26] The AO-FVCOM simulated tidal currents are compared with available Arctic Ocean current measurements (Figure 1) with examples for tidal ellipses shown in Figure 4 for Hudson Bay and in Figure 5 for the Archipelago. The Matlab harmonic analysis toolbox (T\_Tide by Pawlowicz *et al.* [2002]) was used to calculate the tidal current ellipse parameters of both model and measured currents. Harmonic analysis of the field data reveals two facts. First, the ellipse parameters, especially orientation and phase, vary significantly with measurement time for data taken in different seasons and years. At the same location and measurement depth, the difference in orientation and phase for two independent current records can exceed  $45^\circ$  and  $56^\circ$ , respectively. Second, the water depths at some measurement sites are quite different from the model depths constructed using the DBDBV and IBCAO databases. It was shown [Murty, 1985; KP] that, due to the spatial and temporal variations of ice coverage and seasonal/interannual variability in water stratification, the tidal ellipse parameters differ seasonally and from year to year. The tidal motion predicted in this study with AO-FVCOM represents the purely ice-free barotropic case, so that model-data comparisons should be interpreted with caution.

[27] The model-predicted tidal ellipse parameters of major and minor axes are in reasonable agreement with observations in Hudson Strait/Bay and the Canadian Archipelago. Detailed comparisons of model-predicted and observed tidal ellipse parameters are presented in Tables S1–S8 in the auxiliary material, and a summary is given in Table 3. In Hudson Strait/Bay, for example, both model-predicted shape and orientation of the  $M_2$  and  $K_1$  tidal current ellipses are in good agreement with the observations at available measurement sites (Figure 4). Similar results

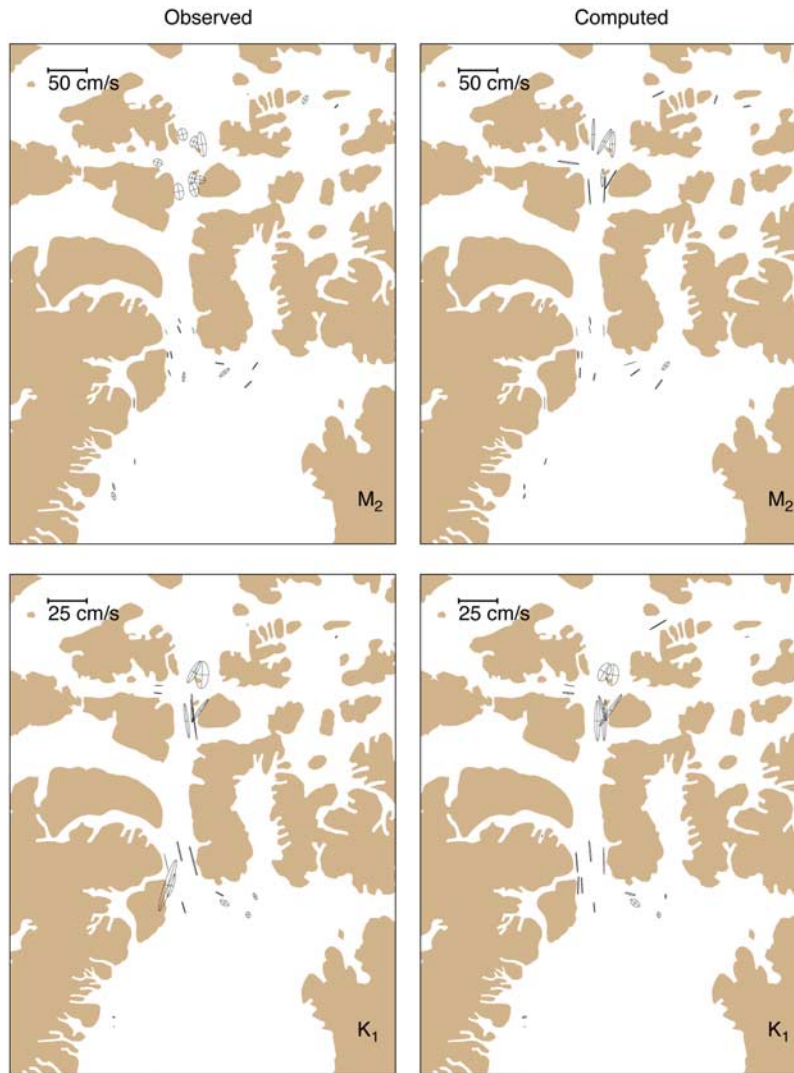


**Figure 5.** Comparison between (left) observed and (right) model-computed  $M_2$  and  $K_1$  tidal ellipses at measurement depths on moorings in the Canadian Archipelago. The measurement depths at those sites differed and are given in Data Sets S7 and S8 in the auxiliary material.

are also found in the Canadian Archipelago (Figure 5). Although the data used in these comparisons were measured at different depths (see Tables S1–S8 in the auxiliary material), the model generally predicts a larger minor axis than measured in both Hudson Strait/Bay and the Canadian Archipelago, which, we believe, is due to the lack of temporal variation of water temperature/salinity and ice in the 3-D barotropic simulations presented here. In these two regions, the model vertical profiles of the ellipse parameters of the semidiurnal and diurnal currents also match reasonably well with measurements. Examples of the model-data comparison are given at sites A ( $71.8188^\circ\text{W}$ ,  $61.9450^\circ\text{N}$ ) in Hudson Strait and B ( $73.6193^\circ\text{W}$ ,  $76.4860^\circ\text{N}$ ) in the northern end of Baffin Bay for  $M_2$  (Figure 6) and at sites C ( $94.0183^\circ\text{W}$ ,  $74.5667^\circ\text{N}$ ) and D ( $93.9117^\circ\text{W}$ ,  $74.4017^\circ\text{N}$ ) in the Canadian Archipelago for  $K_1$  (Figure 7). In the barotropic case, the tidal currents vary slightly in the vertical, except in the bottom boundary layer where the currents decrease rapidly with depth.

[28] The overall errors in simulated tidal currents are relatively small, showing a good model-data agreement in major axes but larger errors in ellipse orientation and phase.

### 3.3. Effects of Stratification

[29] To examine the influence of water stratification on tidal elevation and currents, we reran the tidal simulation by adding the summer climatologic water temperature and salinity fields as an initial condition. The differences in the absolute and RMS errors between the barotropic and stratified cases were relatively small for tidal elevation and the major axis of tidal current ellipses at measurement depths (Table 4), implying that in this case, the average summer stratification has only a weak influence on amplitudes and phases of tidal elevation at coastal tidal measurement sites.

**Table 3.** Comparison Between Model-Predicted and Observed Tidal Current Ellipses Under the Barotropic Condition at 416 Sites<sup>a</sup>

	$M_2$		$S_2$		$K_1$		$O_1$	
	DIFF	RMS	DIFF	RMS	DIFF	RMS	DIFF	RMS
Major axis (cm/s)	4.5	8.3	1.7	2.9	1.2	2.1	0.7	1.4
Orientation (deg)	23.8	32.6	19.9	27.8	31.0	40.6	29.6	39.1
Phase ( $^\circ\text{G}$ )	29.0	36.6	29.2	35.6	32.4	39.3	29.7	37.3

<sup>a</sup>DIFF presents the absolute difference and RMS is the root square mean.

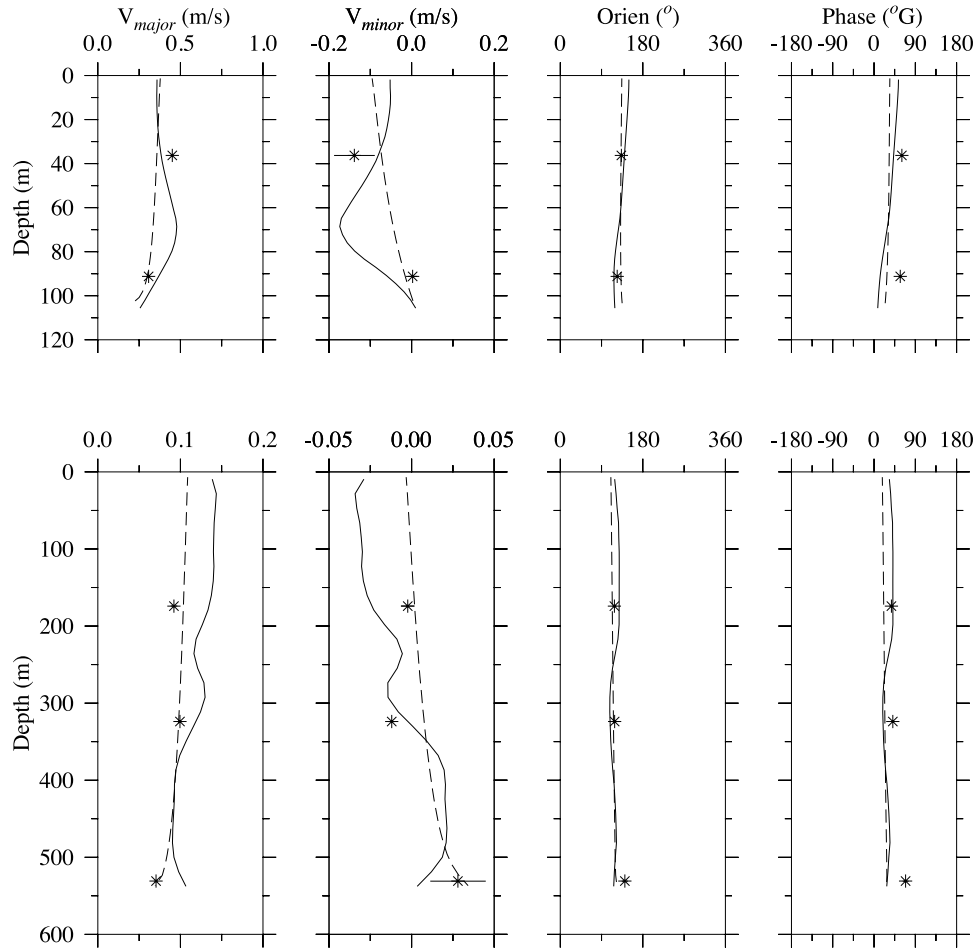


**Figure 6.** Comparison between model-computed (solid line) and observed (symbols) major axes (m/s), minor axes (m/s), orientations (degree), and phases ( $^{\circ}\text{G}$ ) of the  $M_2$  tidal current at (top) site A ( $71.8188^{\circ}\text{W}$ ,  $61.9450^{\circ}\text{N}$ ) in Hudson Strait and (bottom) site B ( $73.6193^{\circ}\text{W}$ ,  $76.4860^{\circ}\text{N}$ ) in the northern end of Baffin Bay. Stars indicate observed; dashed line indicates barotropic; and solid line indicates stratified.

[30] The summer water stratification does change the vertical profile of tidal currents. At sites A and B, for example, both major and minor axes of the  $M_2$  tidal currents exhibit strong vertical shear after the stratification is added (Figure 6). At site C, stratification causes a bottom intensification of the  $K_1$  tidal current (Figure 7), which is consistent with recent high-resolution tidal current measurements made over the Alaska shelf by R. Pickart (personal communication, 2006) and coworkers. It should be noticed here that in Figures 6 and 7, stratification shows little influence on the orientation and phase of both semidiurnal and diurnal tidal currents, consistent with Table 4.

#### 4. Tidal Energy Flux and Tidal Mixing Fronts

[31] The tidal energy flux is estimated using the following definition

$$E_{\lambda} = \frac{1}{T} \int_0^T \rho u D \left[ \frac{u^2 + v^2}{2} + g\zeta \right] dt ;$$

$$E_{\theta} = \frac{1}{T} \int_0^T \rho v D \left[ \frac{u^2 + v^2}{2} + g\zeta \right] dt, \quad (1)$$

where  $E_{\lambda}$  and  $E_{\theta}$  are the zonal and meridional components of the tidal energy flux vector,  $u$  and  $v$  are the zonal and meridional components of the tidal velocity,  $D$  is the total water depth,  $\zeta$  is the tidal elevation,  $\rho$  is the water density,  $g$  is gravity and  $T$  is the tidal period [Crawford, 1984; Kowalik and Proshutinsky, 1993]. The spatial patterns of the semidiurnal  $M_2$  (Figure 8) and  $S_2$  (not shown) tidal energy fluxes are very similar, even though the  $M_2$  tidal energy is, in general, 1 order of magnitude larger than the  $S_2$  tidal energy. The  $K_1$  (Figure 9) and  $O_1$  (not shown) energy fluxes have the same order of magnitude, but their spatial distributions differ in many regions. The distinction between the semidiurnal and diurnal tidal energy fluxes is expounded below based on the  $M_2$  and  $K_1$  tidal waves. The high-resolution AO-FVCOM reveals many mesoscale patterns which vary greatly over space and are difficult to illustrate in a single vector plot over the entire computational domain. Instead, we draw two figures showing the schematic patterns of the  $M_2$  and  $K_1$  tidal energy fluxes, and then give some examples in selected regions.

##### 4.1. $M_2$ Tide

[32] The  $M_2$  tidal energy in the Arctic Ocean is supplied mainly by the progressive tidal wave propagating in from

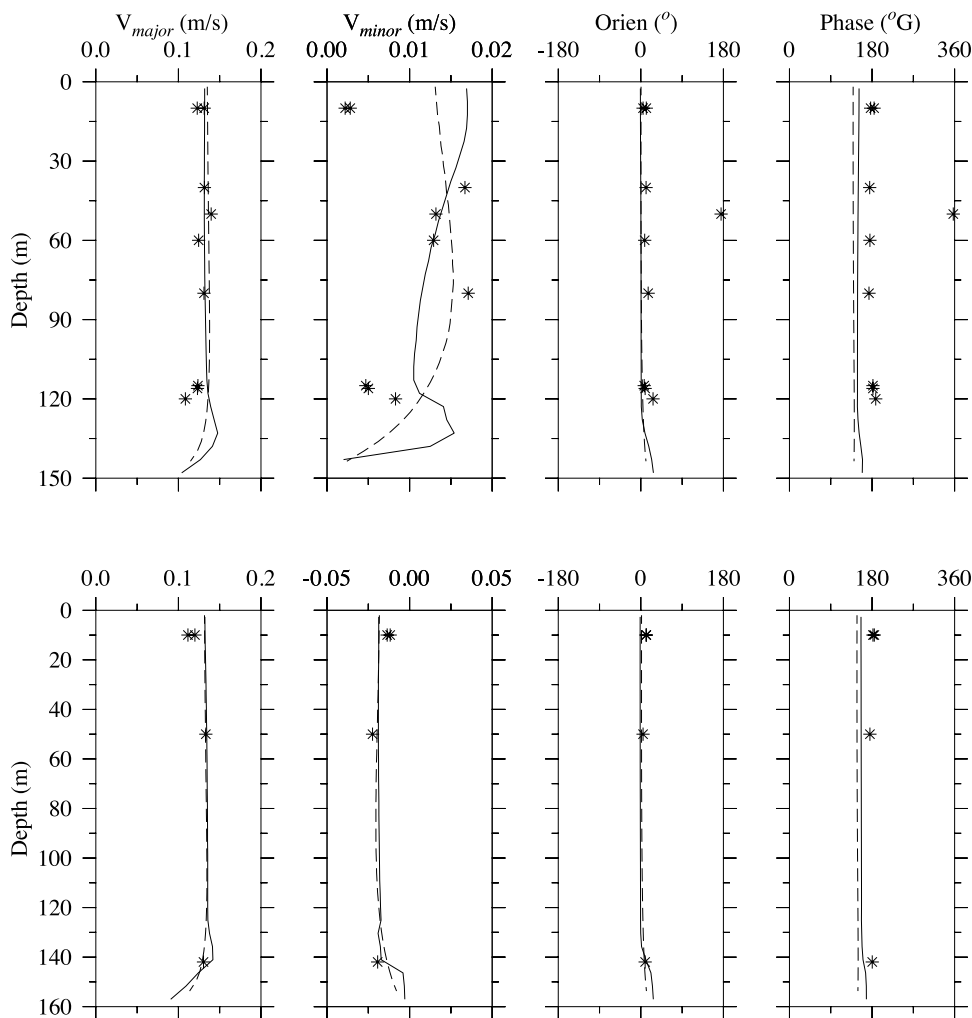


**Figure 7.** Comparison between model-computed (solid line) and observed (symbols) major axes (cm/s), minor axes (m/s), orientations (degree), and phases ( $^{\circ}G$ ) of the  $K_1$  tidal currents at (top) site C ( $94.0183^{\circ}W$ ,  $74.5667^{\circ}N$ ) and (bottom) site D ( $93.9117^{\circ}W$ ,  $74.4017^{\circ}N$ ) in the Canadian Archipelago. Stars indicate observed; dashed line indicates Barotropic; and solid line indicates stratified.

the North Atlantic Ocean (Figure 8). One branch enters Hudson Strait through the Labrador Sea and continues into Hudson Bay with a small portion flowing into Baffin Bay. The other branch flows northward along the eastern North Atlantic Ocean, with one part turning cyclonically and southward along Greenland and the rest continuing northward into the Norwegian Sea and then into the White Sea. The clockwise energy flux around Iceland is fed from the cyclonic branch southeast of Greenland. The Hudson Bay/Strait and White Sea are two regions with large energy dissipation as indicated by the convergence of the  $M_2$  energy flux into these areas.

[33] The  $M_2$  tidal energy in Baffin Bay is about 1 order of magnitude smaller than that in Hudson Strait. It is transferred northward through two paths. One is in the interior, which is the main source of the energy entering the Archipelago and Nares Strait. The other is trapped in the nearshore region along Greenland.

[34] The Canadian Archipelago is a dissipation region for  $M_2$  tidal energy entering from Baffin Bay and the interior of the Arctic Ocean, with Baffin Bay supplying most of the

energy flux for the Archipelago. In this region, the path of the  $M_2$  energy flux is controlled by the intricate island geometry and bathymetry, with flushing through narrow channels and splitting around islands. In Nares Strait, where the Baffin Bay and Arctic Basin fluxes meet, the resultant energy flux vectors form a series of topography-trapped structures indicating a high level of energy dissipation.

**Table 4.** Difference in Tidal Elevation and Currents Predicted by Barotropic and Stratified Model Runs<sup>a</sup>

	$M_2$		$S_2$		$K_1$		$O_1$	
	$ \Delta $	$\Delta_{RMS}$						
<i>Tidal Elevation, Station 257</i>								
Amplitude (cm)	0.4	0.0	0.0	0.0	-0.2	0.0	0.0	-0.1
Phase ( $^{\circ}G$ )	0.4	0.6	-0.5	-1.0	-4.3	-2.6	-2.3	-2.6
<i>Tidal Current Ellipses, Station 416</i>								
Major axis (cm/s)	0.9	1.6	0.2	0.3	0.0	0.1	0.0	-0.1
Orientation ( $^{deg}$ )	4.5	4.6	3.4	4.4	-3.8	-2.9	0.6	1.0
Phase ( $^{\circ}G$ )	6.2	6.5	1.8	2.1	-4.1	-3.1	0.8	1.5

<sup>a</sup>Note that  $|\Delta|$  represents the absolute difference and  $\Delta_{RMS}$  is the difference in the root square mean.

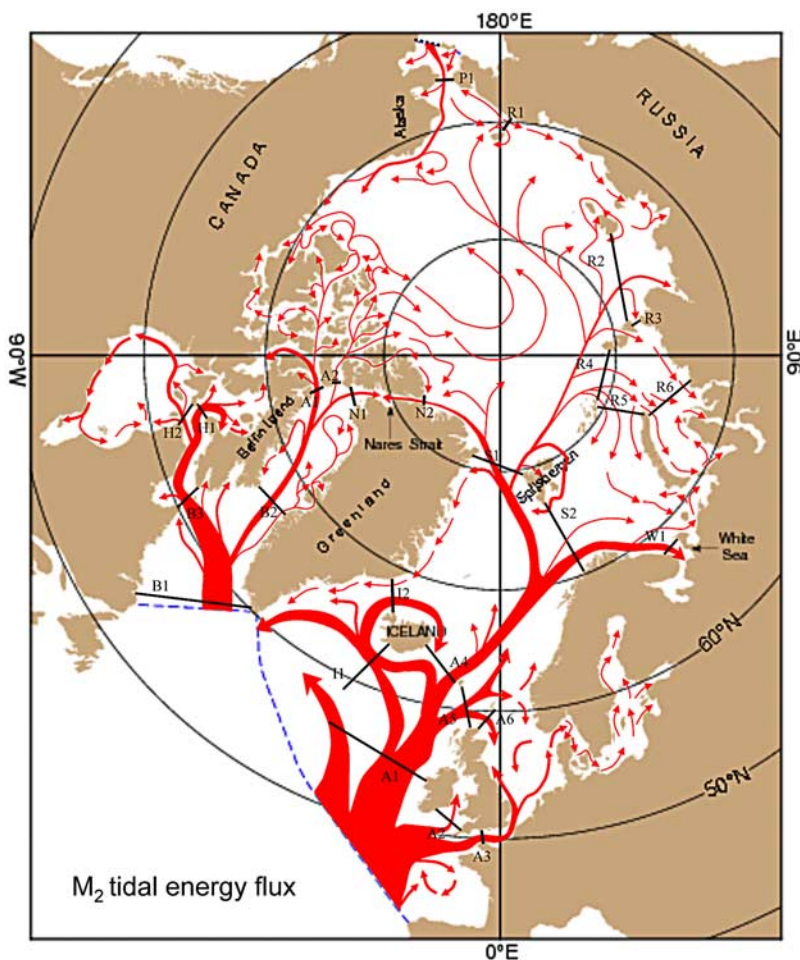


**Figure 8.** The schematic pattern of the model  $M_2$  energy flux in the Arctic Ocean and adjacent coastal regions. Based on the  $M_2$  energy flux vector field predicted by the high-resolution AO-FVCOM. Note that the scale of the line thickness is not proportional to real values.

[35] Around Iceland and Spitsbergen, the  $M_2$  tidal flux vectors exhibit an around-island propagating wave feature. The energy sources of these around-island wave motions are very similar: both come from the cyclonic return flux split from the northward propagating  $M_2$  tidal wave in the Norwegian Sea east of these two islands. Spitsbergen is composed of several islands, between which are channels that exhibit the clockwise flux of  $M_2$  tidal energy.

[36] There is a net  $M_2$  tidal energy flux entering the Arctic through Bering Strait from the Pacific Ocean. A large portion of this energy propagates along the Alaska coast, although the model did show an energy path to the interior and Russian coast after it enters the Arctic region.

#### 4.2. $K_1$ Tide

[37] The  $K_1$  energy flux pattern in the Arctic Ocean is controlled in general by the local bottom topography, with stronger fluxes on the continental slope and weaker in the central basins and near the coast (Figure 9). The energy flux vectors on the continental slope resemble multiple topography-trapped cyclonic and anticyclonic flow structures, which act like retention zones with relatively large tidal dissipation. These trapped waves are amplified at bottom irregularities and strongly dissipated in the same regions

[Lam, 1999; Kowalik and Proshutinsky, 1993; Proshutinsky, 1988]. The AO-FVCOM  $K_1$  tidal energy flux supports the previous KP finding that the energetic tidally averaged diurnal energy flux over the slope is characteristic of shelf waves in the diurnal frequency band generated by astronomical forcing and advected from remote regions. The structure of our model  $K_1$  tidal energy flux is also consistent with theory described by Cartwright [1969] and measurements made in the Weddell Sea, Southern Ocean, by Middleton *et al.* [1987]. These topography-trapped current patterns at the slope form as a result of the interaction of diurnal tidal currents with local bathymetry.

[38] Baffin Bay is one of the main sources for the  $K_1$  tidal wave in the Canadian Archipelago and Nares Strait. In this region, the  $K_1$  energy flux propagates along the eastern slope of the Bay and then much of it enters the straits of the Canadian Archipelago through the northern end of the Bay. Vortices form as a result of the interaction of tidal currents with local steep bottom topography. These vortices have scales in a range of  $\sim 70$ – $200$  km.

[39] The  $K_1$  energy flux in the Canadian Archipelago varies significantly in space. Most of the  $K_1$  energy flux through Parry Channel and Jones Sound comes from Baffin Bay and appears in the region east of  $100^\circ\text{W}$ . A large

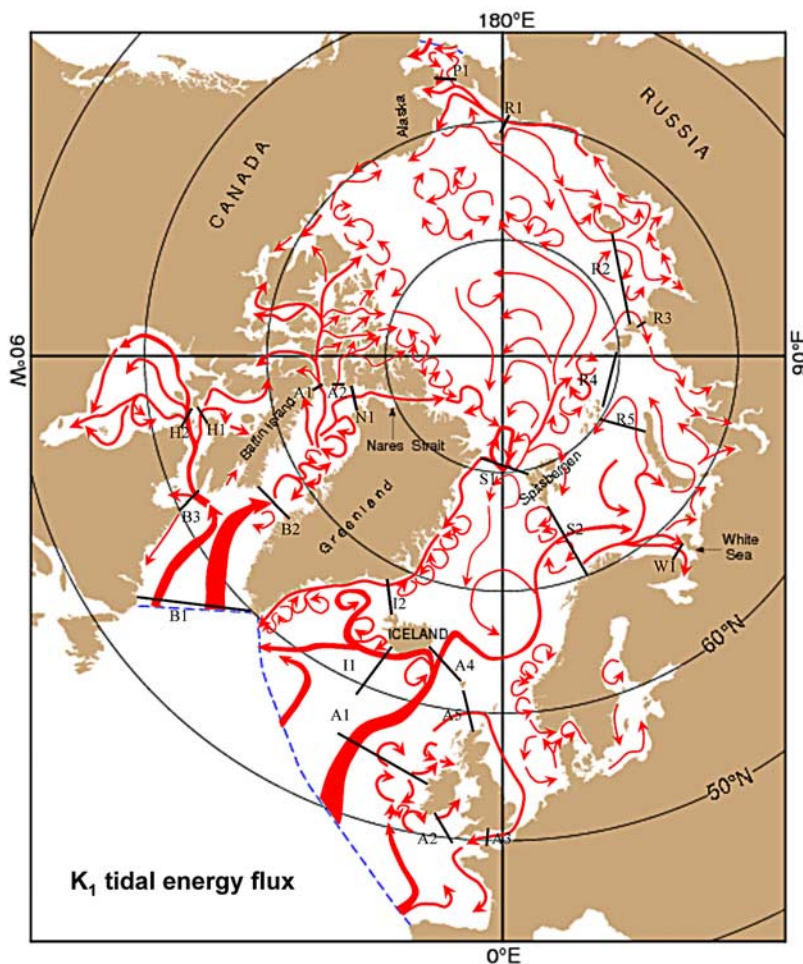


**Figure 9.** The schematic pattern of the model  $K_1$  energy flux in the Arctic Ocean and adjacent coastal regions. Based on the  $K_1$  energy flux vector field predicted by the high-resolution AO-FVCOM. Note that the scale of the line thickness is not proportional to real values.

portion of the incoming energy continues into the Gulf of Boothia and then Committee Bay and the rest splits into Barrow Strait and Wellington Channel around Cornwallis Island. The tidal energy flux which enters Wellington Channel splits around Cornwallis Island and then encounters the energy flux from Jones Sound.

[40] Around Iceland, the  $K_1$  energy flux is much weaker than the  $M_2$  energy flux. Unlike the  $M_2$  tide that propagates clockwise around the island, the  $K_1$  energy flux propagates toward the southeast coast and then splits to west and north, with most of the energy trapped at the shelf break. Trapped shelf waves are also observed at the tip of the steep bottom topography in the northwestern area of the Spitsbergen Islands and no around-island propagating  $K_1$  wave exists.

#### 4.3. Comparison Between $M_2$ and $K_1$ Tidal Energy Fluxes

[41] The spatial patterns of the  $M_2$  and  $K_1$  tidal energy fluxes differ due to the properties of these two tides (Figures 8 and 9). For example, in the Canadian Archipelago, the  $K_1$  tidal energy flux flows southward along islands while the  $M_2$  tidal energy flux rotates cyclonically around islands. Similarly, Nares Strait is a flowthrough channel that transfers  $K_1$  tidal energy from Baffin Bay to

the coast of the Arctic Basin, while Nares Strait is a convergence zone for the  $M_2$  energy fluxes from Baffin Bay and the Arctic Basin. To illustrate the details of the spatial distribution of the  $M_2$  and  $K_1$  tidal energy flux summarized in Figures 8 and 9, here we show the comparison of these two tides in Baffin Bay (Figure 10), the Canadian Archipelago (Figure 11), and around the Spitsbergen (Figure 12). In Baffin Bay, slope-trapped wave patterns are clearly evident for the  $K_1$  tide while the  $M_2$  tide trapped wave is formed around the headland on the northeastern coast near the entrance to Nares Strait. In the Canadian Archipelago, although both  $M_2$  and  $K_1$  tidal energies are mainly from Baffin Bay through the same passages, their propagation patterns within the Archipelago differ significantly. Around the Spitsbergen Islands, the  $M_2$  tidal energy propagates around the islands, while the  $K_1$  tidal energy is mainly trapped at the steep bottom slope region nearby the islands, which is consistent with analytical solutions presented by *Kowalik and Marchenko* [2002]. Both the  $M_2$  and  $K_1$  tides show significant energy exchange through water passages within the islands, which was not resolved in previous Arctic Ocean models.

[42] We calculated the  $M_2$  and  $K_1$  tidal energy fluxes at sections shown in Figures 8 and 9 and compared them with

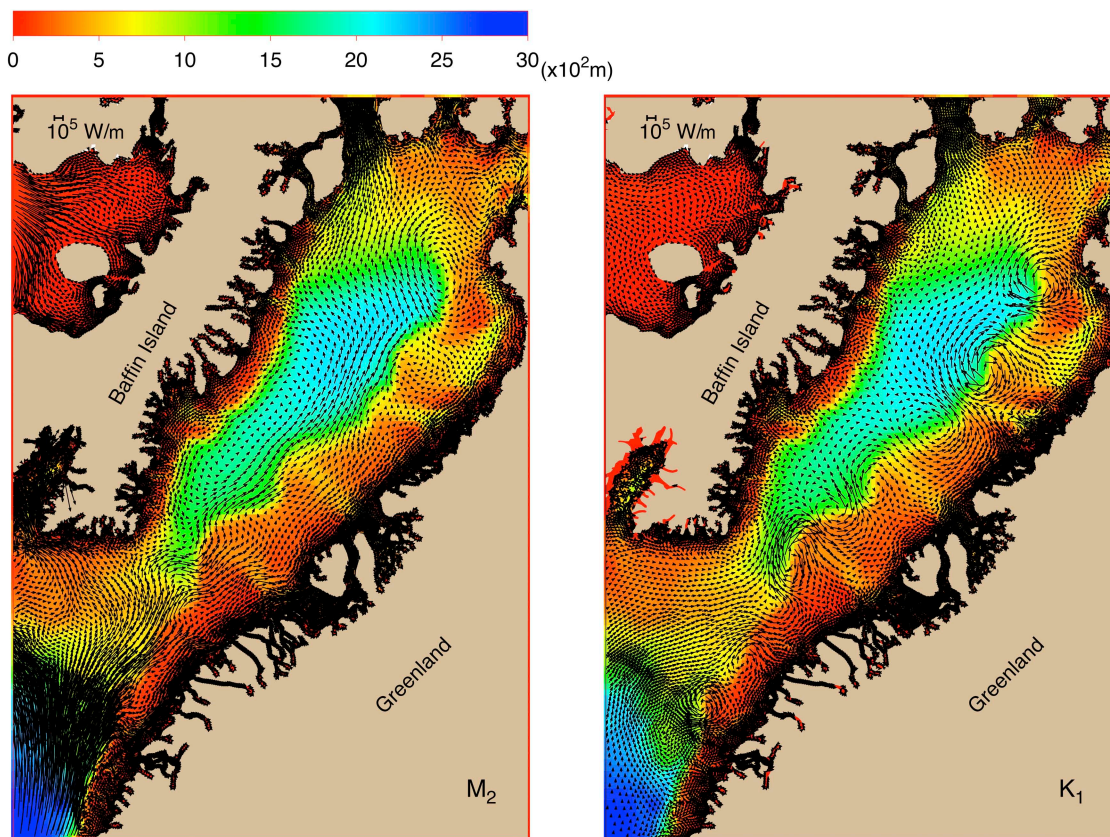


**Figure 10.** Comparison of the model (left)  $M_2$  and (right)  $K_1$  energy flux vectors in Baffin Bay. Plot using the flux values at node points selected in a search radius of 15 km.

KP data and earlier results obtained by *Proshutinsky* [1993]. To be consistent with KP's method, we removed the kinetic energy terms in (1) for the values shown in Table 5. Although AO-FVCOM produces the same order of magnitude fluxes as the KP model in the interior of the Arctic region, the fluxes from these two models differ significantly around the coast and near open boundaries. For example, on section B2, the fluxes predicted by AO-FVCOM and KP are  $18 \times 10^9$  W and  $47 \times 10^9$  W for the  $M_2$  tide, and  $7 \times 10^9$  W and  $12 \times 10^9$  W for the  $K_1$  tide, respectively. On sections N1 and N2 in Nares Strait, AO-FVCOM suggests that Nares Strait is a large tidal dissipation area for the  $M_2$  tidal energy flux that enters the strait from both Baffin Bay and the Arctic continental shelf, while KP showed a  $M_2$  tidal energy flux directed from Baffin Bay to the Arctic region. On section I2 in Denmark Strait, the tidal energies estimated by AO-FVCOM and KP are  $21 \times 10^9$  W and  $19 \times 10^9$  W for the  $M_2$  tide, and are  $2.1 \times 10^9$  W and  $3.7 \times 10^9$  W for the  $K_1$  tide, respectively.

[43] It is not surprising to see a big difference in tidal energy fluxes between AO-FVCOM and KP because they were configured with different horizontal resolutions and geometric fitting. KP used a horizontal resolution of  $\sim 14$  km, while AO-FVCOM's horizontal resolution near the coast was  $\sim 1$ –5 km or less.

#### 4.4. Tidal Mixing Fronts

[44] For the case in which wind mixing, horizontal advection, surface cooling, and freshwater input are not

included, vertical mixing in coastal waters is controlled primarily by a competition between the net surface buoyancy flux produced by solar radiation and kinetic energy dissipation caused by oscillating tidal currents. A mixed region is formed when tidal energy dissipation is stronger than the buoyancy input. In turn, the water column will remain stratified when the surface buoyancy flux is dominant. The tidal mixing front is defined at the transition zone between mixed and stratified regions where these two processes are balanced. In general, the existence and position of the tidal mixing front can be predicted using a particular value of the ratio of potential energy required for complete vertical mixing and the rate of dissipation of mechanical energy due to tidal currents. This ratio is called the tidal mixing efficiency defined by the parameter  $H/U^3$  or  $\log_{10}(H/D_t)$ , where  $H$  is the local water depth,  $U$  a typical tidal current amplitude, and  $D_t$  the tidal kinetic energy dissipation rate ( $D_t = \frac{3}{4}\pi\rho C_d U^3$  where  $C_d$  is the bottom drag coefficient) [Simpson and Hunter, 1974; Loder and Greenberg, 1986; Chen et al., 1995, 2001]. The separation zone between mixed and stratified regions usually coincides with the contour of  $\log_{10}(H/D_t) = 1.9$  to 2.1.

[45] In the Arctic Ocean, the map of  $D_t$  (Figure 13) is consistent with the tidal energy flux pattern. For the case with only the  $M_2$  tide, large  $D_t$  appears along the coast of Hudson Strait/Bay, in Foxe Basin, within England Channel/Strait of Dover, and in the White Sea where large tidal elevations are observed. According to the model-predicted contour of  $\log_{10}(H/D_t) = 2.1$ , these regions should be well

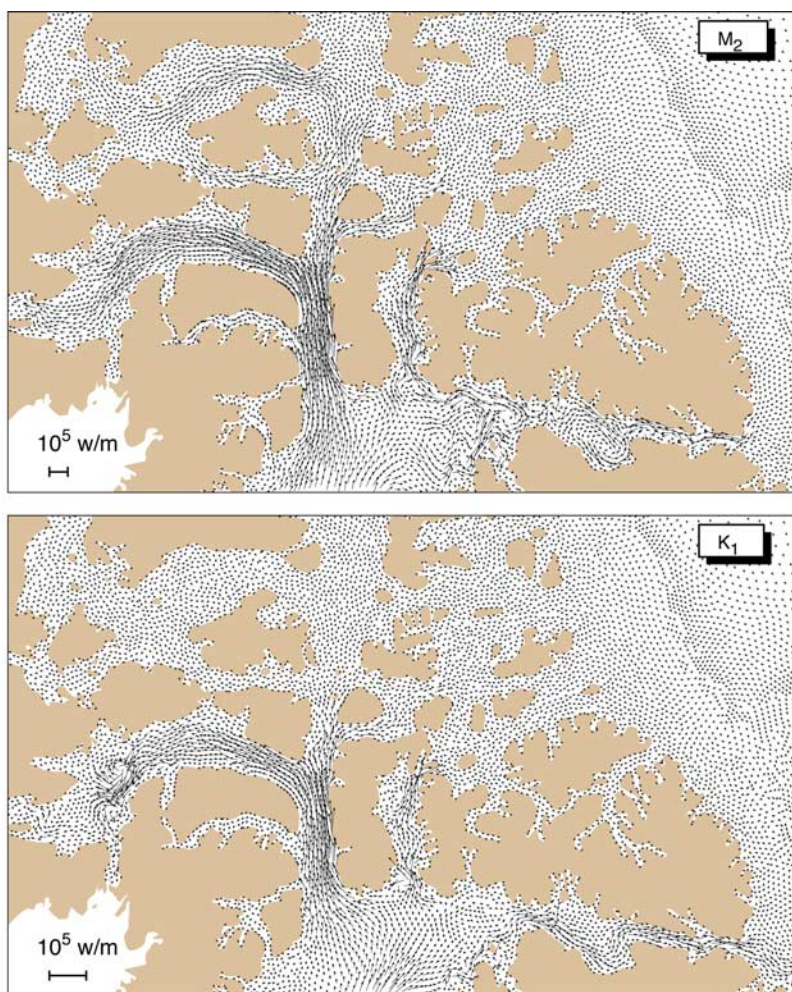


**Figure 11.** Comparison of the model (top)  $M_2$  and (bottom)  $K_1$  energy flux vectors in the Canadian Archipelago. Plot using the flux values at node points selected in a search radius of 10 km. The names of locations described in the text are given in Figure S11 in the auxiliary material.

mixed vertically. When the  $S_2$ ,  $K_1$  and  $O_1$  constituents are added, the energetic tidal dissipation areas are extended offshore to cover the shelf slope. The Gulf of Boothia-Committee Bay in the Canadian Archipelago is a main dissipation region for the diurnal tidal energy transferred from Baffin Bay.

## 5. Discussion

[46] The AO-FVCOM is also validated by comparing with the previous finite difference model KP and PE results. PE divided the Arctic Ocean into seven subregions in their model-data comparisons. Following the same approach, Table 6 provides an intermodel comparison of the surface elevation between KP, PE and AO-FVCOM. In general, the AO-FVCOM results show similar RMS differences as the PE inverse assimilation model and smaller RMS differences than other tidal simulation models. These AO-FVCOM experiments clearly show that resolving coastal geometry and slope bathymetry can significantly improve the accuracy of tidal simulation in the Arctic region. The AO-FVCOM provides smaller RMS errors than all previous 2-D dynamics-based tidal model results. With these improvements,

data assimilation is not needed for AO-FVCOM to reach the accuracy level as predicted by the PE inverse assimilation tidal model. The importance of geometric fitting can be seen from the tidal simulation in the Canadian Archipelago where many channels and water passages are narrower than 5 km. By resolving the irregular coastal geometry, AO-FVCOM produces a better simulation than the 2-D high-resolution grid (5 km) forward tidal model of PE.

[47] By assimilating available tide gauge data into a tidal model, the inverse approach is able to construct the tidal field with a minimum RMS error relative to the measurements. This approach is suitable for tidal forecast applications, but it is difficult to couple inversed-predicted tides into a real-time ocean-ice model system. In the turbulent dissipative Arctic region, the tidal motion is characterized by a self-restoring system controlled by local geometry and bathymetry, tidal forcing at the open boundary and astronomical forcing at the surface [Chen *et al.*, 2009]. Data assimilation can help us to obtain the best estimation of tidal elevation within a minimum overall RMS error, but it doesn't change the self-restoring nature of tidal motion in this region. This means that when the data assimilation stops, the model field rapidly adjusts back to the original

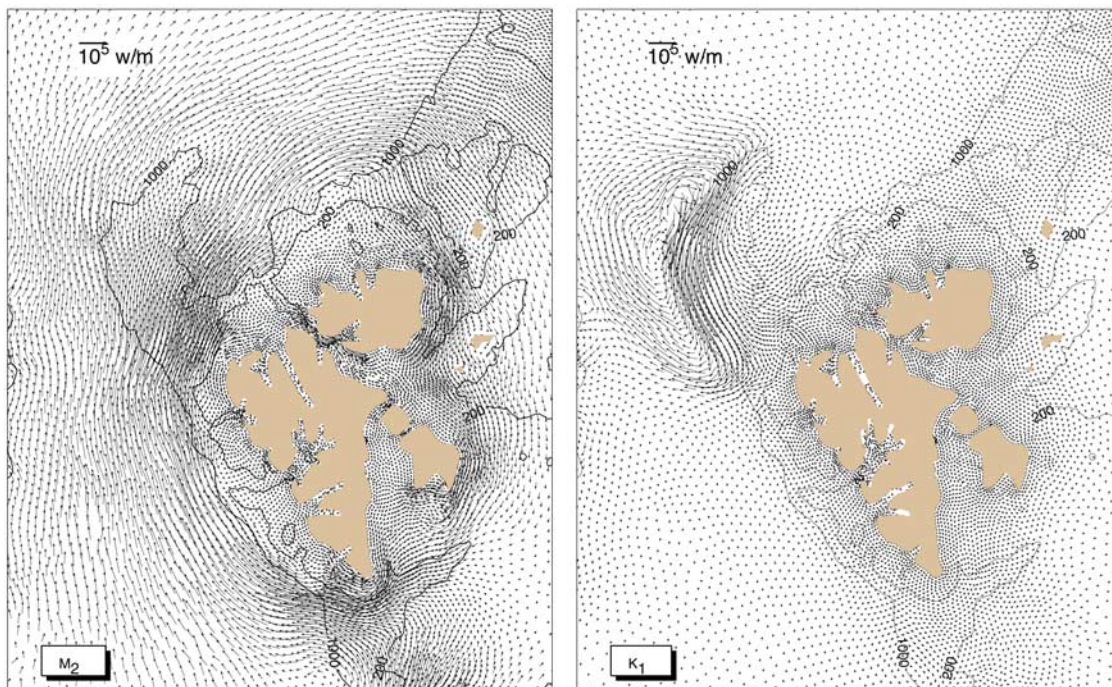


**Figure 12.** Comparison of the model (left)  $M_2$  and (right)  $K_1$  energy flux vectors around Spitsbergen Islands. Plot using the flux values at node points selected in a search radius of 10 km.

solution before assimilation. While the inverse data assimilation provides accurate tidal prediction for practical purposes, an effort should be made on improving the model dynamics and bathymetric data to obtain the true tidal motion.

[48] Five new bottom pressure recorders were deployed to measure the tidal elevation in the basin by the Beaufort Gyre Observing System (<http://www.whoi.edu/beaufortgyre/>) and the North Pole Environmental Observatory (<http://psc.apl.washington.edu/northpole/>). Four are located in the Beaufort Gyre region and one at the North Pole. The time series of surface elevation were available at four of these sites shown in Table 7. Since these data were not assimilated in the PE inverse model, they provide an independent evaluation of the model performance. Table 7 shows a model-data comparison of tidal constants predicted by AO-FVCOM and the PE inverse assimilation model at the four sites, in which the model-data RMS errors were estimated separately for the amplitudes and phases and the same RMS analysis were used for both models. The results indicate that AO-FVCOM provided a more accurate tidal simulation in the interior of the Arctic Ocean, but both models show relatively large phase errors. It is not surprising that the models failed to capture the tidal phases in that area, because these measurement sites are in the vicinity of the major Arctic Ocean amphidromic points and the phases vary significantly with stratification and ice coverage.

[49] Accurate prediction of tidal currents is required to solve different problems of both scientific and practical importance in the Arctic Ocean. Knowledge of tidal currents can guide the prediction of navigation conditions, sea ice internal stresses and ridging. Tidal current prediction is also useful for removal of tidal signals from short-term shipboard current measurement data, analysis of tidal mixing and

determination of origin of internal waves. In order to predict tidal currents, however, tidal constituents have to be known from observations. Because of severe weather conditions,

**Table 5.** Tidal Energy Flux on Selected Section for  $M_2$  and  $K_1$  Tidal Constituents<sup>a</sup>

Section	$M_2$ ( $10^9$ W)		$K_1$ ( $10^8$ W)	
	FVCOM	KP	FVCOM	KP
A1	264	201	42	19.1
A2	23		0.7	
A3	57		2	
A4	27		6	
A5	75		6	
A6	16		3	
B1	306		99	
B2	18	46.7	69	115.0
B3	276		3	
H1	53		0.3	
H2	120		2	
I1	125		19	
I2	21	19.1	21	37.1
N1	1	2.8	9	
N2	1		7	
A1	9	1.8	29	
A2	3	6.3	9	
P1	0.1		0.1	0.2
R1	0.1			
R2	2		0.4	
R3	0.4	<0.1	0.3	
R4	4	9.1	4	
R5	3	3.8	2	
R6	1	3.4	0.4	5.0
S1	25	32.8	11	43.5
S2	55	43.3	4	4.8
W1	39	29.3	1	16.9

<sup>a</sup>Note: values listed here do not include the flux direction.

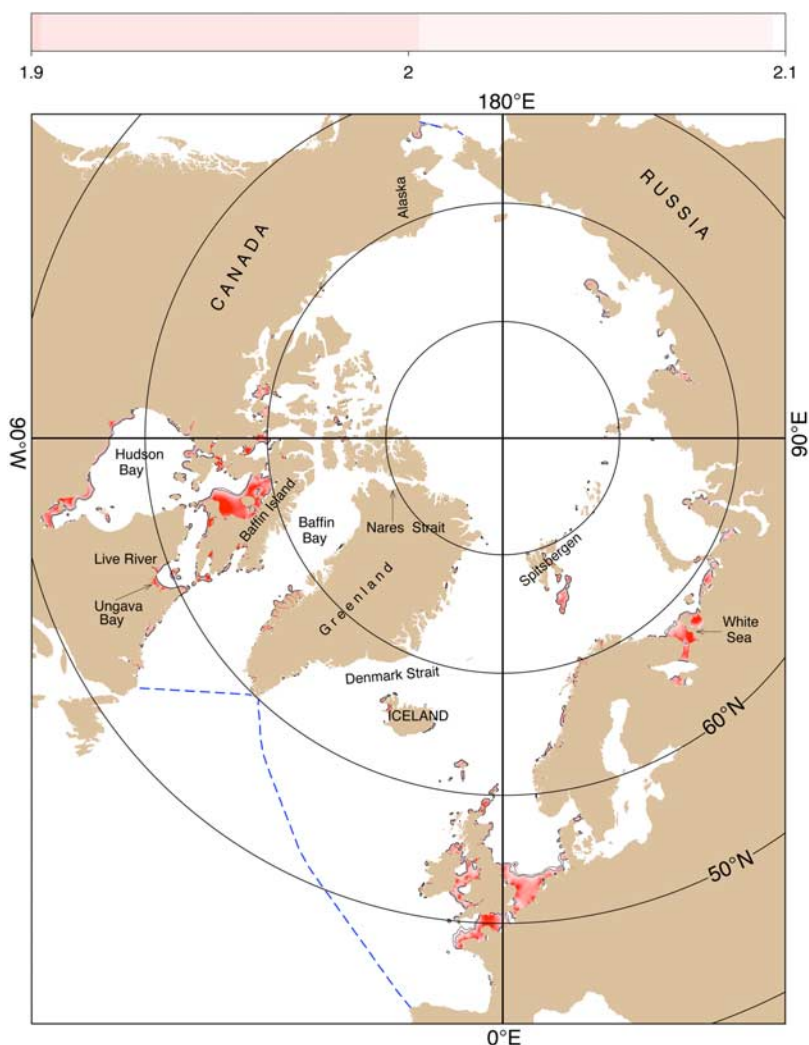


**Figure 13.** Plot of the tidal mixing parameter  $\log_{10}(H/D_t)$  (see text for definition) computed using the combined  $M_2$ ,  $S_2$ ,  $K_1$  and  $O_1$  tidal current velocities. Solid line is the contour of  $\log_{10}(H/D_t) = 2.1$ .

seasonal and year-round coverage of sea ice, and the high cost of field measurements, there are insufficient current data available to build the tidal constituent database for direct tidal current prediction in much of the Arctic Ocean. However, the available current measurements do provide a good database to compare with tidal models and make the model-based tidal current prediction more reliable.

[50] In general, barotropic tidal currents can be predicted with high accuracy [Pugh, 1987; Foreman *et al.*, 1995]. In the Arctic Ocean, the baroclinic (internal) tidal currents are essential and sometimes dominate the total kinetic tidal energy [e.g., Danielson and Kowalik, 2005], although our study shows that their contributions to the tidal elevation are small. Because internal tides in the Arctic Ocean are highly intermittent, it is a challenge whether they can be accurately predicted by a model without realistic information of water stratification [Wunsch, 1975; Munk, 1997; Feng *et al.*, 1998; Morozov, 1995; Müller and Briscoe, 1999]. In the Arctic Ocean, the problem is even more complicated because of drifting and land fast ice. A reasonable agreement in magnitudes but not in orientations and phases between AO-FVCOM predicted and observed tidal cur-

rents suggest that it would be impossible for a model to reproduce realistic internal tides without accurate simulation of water stratification and ice in the Arctic Ocean. On the other hand, AO-FVCOM did resolve the spatial variation patterns of tidal currents measured around the North Pole, in the Barents Sea near Spitsbergenbanken, Bear and Hopen Islands, along the North Siberian Shelf in the White Sea and along the Alaska Beaufort shelf [Aagaard, 1981; Huthnance, 1981; Nilsen *et al.*, 1990; Kowalik and Proshutinsky, 1995].

[51] We also investigated the impact of model horizontal resolution on the accuracy of the Arctic Ocean tidal simulations. The first AO-FVCOM grid was configured with a horizontal resolution of  $\sim 2-4$  km in the Canadian Archipelago, inlets, and narrow straits/channels to  $\sim 25-30$  km in the interior [Gao *et al.*, 2006]. We refer to this as the “low-resolution” grid in relation to the “high-resolution” grid used in this study. The tidal elevation difference between high- and low-resolution AO-FVCOM simulations is small in both amplitudes and phases; the overall root-mean-square difference in amplitude is 1.0 cm and phase is  $3^\circ$ . This difference is insignificant compared with the measurement



**Table 7.** Observed and Simulated Tidal Amplitudes and Phases Based on Data From Four Bottom Pressure Recorders and FVCOM and AOTIMS

	Locations							
	150°W, 75°N		150°W, 78°N		140°W, 77°N		0°W, 90°N	
	Amp (cm)	Phase (°G)	Amp (cm)	Phase (°G)	Amp (cm)	Phase (°G)	Amp (cm)	Phase (°G)
				$K_1$				
Observed	1.6	145	1.4	100	0.9	122	2.7 ± 0.3	339 ± 0.5
FVCOM	0.2	247	1.2	315	1.2	7	3.3	328
AOTIMS	(3.0)	(265)	(2.6)	(273)	(1.6)	(266)	(1.8)	(326)
				$O_1$				
Observed	2.3	182	1.5	179	1.6	188	1.8 ± 0.2	325 ± 0.7
FVCOM	1.8	179	1.2	196	1.1	178	1.5	326
AOTIMS	(2.9)	(238)	(2.4)	(241)	(2.1)	(232)	(1.2)	(318)
				$M_2$				
Observed	4.5	267	4.1	271	3.3	265	6.5 ± 0.2	60 ± 0.2
FVCOM	4.0	257	2.8	261	3.9	266	6.0	53
AOTIMS	(2.7)	(267)	(1.9)	(256)	(2.7)	(272)	(5.0)	(63)
				$S_2$				
Observed	2.2	313	1.7	323	1.4	315	2.8 ± 0.3	111 ± 0.5
FVCOM	1.7	305	1.0	311	1.4	320	2.5	113
AOTIMS	(1.6)	(329)	(1.0)	(327)	(1.3)	(335)	(2.4)	(124)

the complex coastal geometry may lead to errors in the magnitude and direction of energy flow in the Canadian Archipelago.

[54] The comparison of the model-simulated tidal elevations for homogenous and summer climatologic stratification cases suggests that water stratification influences the vertical distribution of tidal currents but not the water transport and thus tidal elevation. A reasonable model-data agreement in magnitudes but not in orientations and phases suggest that it would be impossible for a model to reproduce realistic tides in the Arctic Ocean without accurate simulation of water stratification and ice. It is a challenge for a model since it involves internal tides that can vary intermittently and complex ice dynamics.

[55] **Acknowledgments.** This research was supported by the NSF Office of Polar Programs through grants OPP ARC-0712903, ARC-0732084, and ARC-0804029 for C. Chen, G. Gao, and G. Cowles; OPP ARC-0804010 and ARC-0712848 for A. Proshutinsky; OPP ANT-0523223, ARC0712848, NOAA Cooperative Agreement NA17RJ1223 (409) and the WHOI Smith Chair for R. C. Beardsley. J. Qi was supported by the SMAST fishery program under NOAA grants NA04NMF4720332 and NA05NMF4721131. The spherical coordinate version of FVCOM was developed with initial funds from NSF grants OCE-0606928 and OCE-0726851. Gao was also supported by the Chinese NSF Arctic Ocean grant under contract 40476007. Any opinions, findings, and conclusions or recommendations expressed in this material are those of the authors and do not necessarily reflect the views of the National Science Foundation. We want to acknowledge the generous help provided by L. Padman, who clarified the different methods used to compute the model-data RMS differences and made other important suggestions to improve this work, and the input of two anonymous reviewers that also helped us improve this paper. This is the School of Marine Science and Technology (SMAST)/University of Massachusetts-Dartmouth contribution 09-0701.

## References

- Aagaard, K. (1981), On the deep circulation in the Arctic Ocean, *Deep Sea Res., Part A*, 28(3), 251–268, doi:10.1016/0198-0149(81)90066-2.
- Cartwright, D. E. (1969), Extraordinary tidal currents near St Kilda, *Nature*, 223, 928–932, doi:10.1038/223928a0.
- Chen, C., R. C. Beardsley, and R. Limeburner (1995), Variability of currents in late spring in the northern Great South Channel, *Cont. Shelf Res.*, 15, 451–473, doi:10.1016/0278-4343(94)00056-S.
- Chen, C., R. C. Beardsley, and P. J. S. Franks (2001), A 3-D prognostic model study of the ecosystem over Georges Bank and adjacent coastal

- regions. Part I: Physical model, *Deep Sea Res., Part II*, 48, 419–456, doi:10.1016/S0967-0645(00)00124-7.
- Chen, C., H. Liu, and R. C. Beardsley (2003), An unstructured, finite-volume, three-dimensional, primitive equation ocean model: Application to coastal ocean and estuaries, *J. Atmos. Oceanic Technol.*, 20, 159–186, doi:10.1175/1520-0426(2003)020<0159:AUGFVT>2.0.CO;2.
- Chen, C., R. C. Beardsley, and G. Cowles (2006a), An unstructured grid, finite-volume coastal ocean model (FVCOM) system, *Oceanography*, 19(1), 78–89.
- Chen, C., R. C. Beardsley, and G. Cowles (2006b), An unstructured grid, finite-volume coastal ocean model-FVCOM user manual, *Tech. Rep. SMAST/UMASSD-06-0602*, 2nd ed., 318 pp., Sch. for Mar. Sci. and Technol., Univ. of Mass. Dartmouth, New Bedford.
- Chen, C., H. Huang, R. C. Beardsley, H. Liu, Q. Xu, and G. Cowles (2007), A finite-volume numerical approach for coastal ocean circulation studies: Comparisons with finite-difference models, *J. Geophys. Res.*, 112, C03018, doi:10.1029/2006JC003485.
- Chen, C., P. Malanotte-Rizzoli, J. Wei, R. C. Beardsley, Z. Lai, P. Xue, S. Lyu, Q. Xu, J. Qi, and G. W. Cowles (2009), Application and comparison of Kalman filters for coastal ocean problems: An experiment with FVCOM, *J. Geophys. Res.*, 114, C05011, doi:10.1029/2007JC004548.
- Cowles, G. (2008), Parallelization of the FVCOM Coastal Ocean Model, *Int. J. High Perform. Comput. Appl.*, 22(2), 177–193, doi:10.1177/1094342007083804.
- Crawford, W. R. (1984), Energy flux and generation of diurnal shelf waves along Vancouver Island, *J. Phys. Oceanogr.*, 14, 1600–1607, doi:10.1175/1520-0485(1984)014<1600:EFAGOD>2.0.CO;2.
- Danielson, S., and Z. Kowalik (2005), Tidal currents in the St. Lawrence Island region, *J. Geophys. Res.*, 110, C10004, doi:10.1029/2004JC002463.
- D’Asaro, E. A., and J. M. Morison (1992), Internal waves and mixing in the Arctic Ocean, *Deep Sea Res., Part A*, 39(2), S459–S484, doi:10.1016/S0198-0149(06)80016-6.
- Feng, M., M. A. Merrifield, R. Pinkel, P. Hacker, A. J. Plueddemann, E. Firing, and C. Eriksen (1998), Semidiurnal tides observed in the western equatorial Pacific during the Tropical Ocean-Global Atmosphere Response Experiment, *J. Geophys. Res.*, 103(C5), 10,253–10,272, doi:10.1029/98JC00264.
- Foreman, M. G. G., W. R. Crawford, and R. F. Marsden (1995), De-tiding: Theory and practice, in *Quantitative Skill Assessment for Coastal Ocean Models, Coastal Estuarine Stud.*, vol. 47, edited by D. R. Lynch and A. M. Davies, pp. 203–239, AGU, Washington, D. C.
- Galperin, B., L. H. Kantha, S. Hassid, and A. Rosati (1988), A quasi-equilibrium turbulent energy model for geophysical flows, *J. Atmos. Sci.*, 45, 55–62, doi:10.1175/1520-0469(1988)045<0055:AQETEM>2.0.CO;2.
- Gao, G., C. Chen, H. Huang, J. Qi, A. Proshutinsky, and R. C. Beardsley (2006), A new unstructured grid, finite-volume Arctic Ocean model (FVCOM-Arctic): Impacts of geometric fitting on circulation, *Eos Trans. AGU*, 87(36), Ocean Sci. Meet. Suppl., Abstract OS350-17.

- Golubeva, E. N., and G. A. Platov (2007), On improving the simulation of Atlantic Water circulation in the Arctic Ocean, *J. Geophys. Res.*, *112*, C04S05, doi:10.1029/2006JC003734.
- Holloway, G., and A. Proshutinsky (2007), Role of tides in Arctic ocean/ice climate, *J. Geophys. Res.*, *112*, C04S06, doi:10.1029/2006JC003643.
- Huthnance, J. M. (1981), On mass transport generated by tides and long waves, *J. Fluid Mech.*, *102*, 367–387, doi:10.1017/S0022112081002693.
- Joyce, T., and A. Proshutinsky (2007), Greenland's island rule and the Arctic Ocean circulation, *J. Mar. Res.*, *65*, 639–653, doi:10.1357/002224007783649439.
- Kowalik, Z., and A. Marchenko (2002), Tidal motion enhancement around islands, *J. Mar. Res.*, *60*, 551–581, doi:10.1357/002224002762324211.
- Kowalik, Z., and A. Proshutinsky (1993), Diurnal tides in the Arctic Ocean, *J. Geophys. Res.*, *98*(C9), 16,449–16,468, doi:10.1029/93JC01363.
- Kowalik, Z., and A. Proshutinsky (1994), The Arctic Ocean tides, in *The Polar Oceans and Their Role in Shaping the Global Environment*, *Geophys. Monogr. Ser.*, vol. 85, edited by O. M. Johannessen et al., pp. 137–158, AGU, Washington, D. C.
- Kowalik, Z., and A. Proshutinsky (1995), Topographic enhancement of tidal motion in the western Barents Sea, *J. Geophys. Res.*, *100*(C2), 2613–2637, doi:10.1029/94JC02838.
- Kulikov, E. A., A. B. Rabinovich, and E. C. Carmack (2004), Barotropic and baroclinic tidal currents on the Mackenzie shelf break in the south-eastern Beaufort Sea, *J. Geophys. Res.*, *109*, C05020, doi:10.1029/2003JC001986.
- Kwok, R., H. J. Zwally, and D. Yi (2004), ICES at observations of Arctic sea ice: A first look, *Geophys. Res. Lett.*, *31*, L16401, doi:10.1029/2004GL020309.
- Lam, F.-P. A. (1999), Shelf waves with diurnal tidal frequency at the Greenland shelf edge, *Deep Sea Res., Part I*, *46*, 895–923, doi:10.1016/S0967-0637(98)00090-9.
- Loder, J. W., and D. A. Greenberg (1986), Predicted positions of tidal fronts in the Gulf of Maine region, *Cont. Shelf Res.*, *6*, 397–414, doi:10.1016/0278-4343(86)90080-4.
- Mellor, G. L., and T. Yamada (1982), Development of a turbulence closure model for geophysical fluid problem, *Rev. Geophys. Space Phys.*, *20*, 851–875, doi:10.1029/RG020i004p00851.
- Middleton, J. H., T. D. Foster, and A. Foldvick (1987), Diurnal shelf waves in the southern Weddell Sea, *J. Phys. Oceanogr.*, *17*, 784–791, doi:10.1175/1520-0485(1987)017<0784:DSWITS>2.0.CO;2.
- Morozov, E. G. (1995), Semidiurnal internal wave global field, *Deep Sea Res., Part I*, *42*, 135–148, doi:10.1016/0967-0637(95)92886-C.
- Muench, R. D., R. K. Dewey, and U. Schauer (1996), Internal waves and vertical mixing over the Laptev Sea slope, in *Proceedings of the ACSYS conference on the dynamics of the Arctic Climate System*, Goteborg, Sweden, 7–10 Nov., 1994, *WMO/TD 760*, pp. 441–445, World Meteorol. Org., Geneva, Switzerland.
- Müller, P., and M. Briscoe (1999), Diapycnal mixing and internal waves, in *Aha Huliko'a: Dynamics of Oceanic Internal Gravity Waves, II*, pp. 289–294, Univ. of Hawaii at Manoa, Honolulu.
- Munk, W. H. (1997), Once again: Once again—tidal friction, *Prog. Oceanogr.*, *40*, 7–35, doi:10.1016/S0079-6611(97)00021-9.
- Munk, W. H., and C. Wunsch (1998), Abyssal recipes II: Energetics of tidal and wind mixing, *Deep Sea Res., Part I*, *45*, 1977–2010, doi:10.1016/S0967-0637(98)00070-3.
- Murty, T. S. (1985), Modification of hydrographic characteristics, tides, and normal modes by ice cover, *Mar. Geod.*, *9*(4), 451–468, doi:10.1080/15210608509379538.
- Nilsen, J. H., T. A. McClimans, and S. M. Lovas (1990), Rift drift in floe flow: Iceberg wakes in the Arctic Sea ice, *Cont. Shelf Res.*, *10*, 81–86, doi:10.1016/0278-4343(90)90036-L.
- Padman, L. (1995), Small-scale physical processes in the Arctic Ocean, in *Arctic Oceanography: Marginal Ice Zones and Continental Shelves*, *Coastal Estuarine Stud.*, vol. 49, edited by W. O. Smith Jr. and J. M. Grebmeier, pp. 97–129, AGU, Washington, D. C.
- Padman, L., and T. M. Dillon (1991), Turbulent mixing near the Yermak Plateau during the Coordinated Eastern Arctic Experiment, *J. Geophys. Res.*, *96*(C3), 4769–4782, doi:10.1029/90JC02260.
- Padman, L., and S. Erofeeva (2004), A barotropic inverse tidal model for the Arctic Ocean, *Geophys. Res. Lett.*, *31*, L02303, doi:10.1029/2003GL019003.
- Panteleev, G., A. Proshutinsky, M. Kulakov, D. A. Nechaev, and W. Maslowski (2007), Investigation of the summer Kara Sea circulation employing a variational data assimilation technique, *J. Geophys. Res.*, *112*, C04S15, doi:10.1029/2006JC003728.
- Pawlowicz, R., B. Beardsley, and S. Lentz (2002), Classical tidal harmonic analysis with error analysis in MATLAB using TIDE, *Comput. Geosci.*, *28*, 929–937, doi:10.1016/S0098-3004(02)00013-4.
- Pease, C. H., P. Turet, and R. S. Pritchard (1995), Barents Sea tidal and inertial motions from ARGOS ice buoys during the Coordinated Eastern Arctic Experiment, *J. Geophys. Res.*, *100*(C12), 24,705–24,718, doi:10.1029/95JC03014.
- Pietrzak, J. J., B. Jakobson, H. Burchard, H. J. Vested, and O. Petersen (2002), A three-dimensional hydrostatic model for coastal and ocean modeling using a generalized topography following co-ordinate system, *Ocean Modell.*, *4*, 173–205, doi:10.1016/S1463-5003(01)00016-6.
- Prinsenberg, S. J. (1988), Damping and phase advance of the tide in western Hudson Bay by the annual ice cover, *J. Phys. Oceanogr.*, *18*, 1744–1751, doi:10.1175/1520-0485(1988)018<1744:DAPAOT>2.0.CO;2.
- Proshutinsky, A. (1988), Generation of eddy structures in the Faroe-Shetland Strait by tidal currents, *Oceanography*, *28*, 567–571.
- Proshutinsky, A. (1993), *Variability of Sea Level in the Arctic Ocean* (in Russian), 216 pp., Gidrometeoizdat, St. Petersburg.
- Proshutinsky, A., and Z. Kowalik (2007), Preface to special section on Arctic Ocean Model Intercomparison Project (AOMIP) studies and results, *J. Geophys. Res.*, *112*, C04S01, doi:10.1029/2006JC004017.
- Proshutinsky, A., et al. (2001), The Arctic Ocean Model Intercomparison Project (AOMIP), *Eos Trans. AGU*, *82*(51), 637, doi:10.1029/01EO00365.
- Proshutinsky, A., et al. (2005), Arctic Ocean study: Synthesis of model results and observations, *Eos Trans. AGU*, *86*(40), 368, doi:10.1029/2005EO400003.
- Pugh, D. T. (1987), *Tides, Surges and Mean Sea-Level*, 472 pp., John Wiley, Chichester, U. K.
- Robertson, R. (2001), Internal tides and baroclinicity in the southern Weddell Sea: 2. Effects of the critical latitude and stratification, *J. Geophys. Res.*, *106*(C11), 27,017–27,034, doi:10.1029/2000JC000476.
- Schiller, A. (2004), Effects of explicit tidal forcing in an OGCM on the water-mass structure and circulation in the Indonesian throughflow region, *Ocean Modell.*, *6*, 31–49, doi:10.1016/S1463-5003(02)00057-4.
- Simpson, J. H., and J. R. Hunter (1974), Fronts in the Irish Sea, *Nature*, *250*, 404–406, doi:10.1038/250404a0.
- Smagorinsky, J. (1963), General circulation experiments with the primitive equations, I. The basic experiment, *Mon. Weather Rev.*, *91*, 99–164, doi:10.1175/1520-0493(1963)091<0099:GCEWTP>2.3.CO;2.
- St. Laurent, L. (2008), Turbulent dissipation on the margins of the South China Sea, *Geophys. Res. Lett.*, *35*, L23615, doi:10.1029/2008GL035520.
- St. Laurent, L., and C. Garrett (2002), The role of internal tides in mixing the deep ocean, *J. Phys. Oceanogr.*, *32*, 2882–2899, doi:10.1175/1520-0485(2002)032<2882:TROITI>2.0.CO;2.
- Voynov, G. (2002), Tide and tidal streams, in *Polar Seas Oceanography: An Integrated Case Study of the Kara Sea*, pp. 147–214, Springer, New York.
- Wang, J., et al. (2003), Working toward improved small-scale sea ice-ocean modeling in the Arctic seas, *Eos Trans. AGU*, *84*(34), 325, 329–330, doi:10.1029/2003EO340001.
- Wunsch, C. (1975), Internal tides in the ocean, *Rev. Geophys. Space Phys.*, *13*, 167–182, doi:10.1029/RG013i001p00167.
- Zakharchuk, E. A. (1999), Internal waves in the Laptev Sea, in *Land-Ocean System in the Siberian Arctic: Dynamic and History*, edited by H. Kassens et al., pp. 43–51, Springer, New York.

R. C. Beardsley and A. Proshutinsky, Department of Physical Oceanography, Woods Hole Oceanographic Institution, Woods Hole, MA 02543, USA.

C. Chen, G. Cowles, G. Gao, H. Lin, and J. Qi, Department of Fisheries Oceanography, School for Marine Science and Technology, University of Massachusetts-Dartmouth, 706 South Rodney French Boulevard, New Bedford, MA 02748, USA. (c1chen@umassd.edu)

Z. Kowalik, Institute of Marine Science, University of Alaska Fairbanks, Fairbanks, AK 99775, USA.